The Astrophysical Journal, 695:221–237, 2009 April 10 doi:10.1088/0004-637X/695/1/221

PHYSICAL PROPERTIES OF COOLING PLASMA IN QUIESCENT ACTIVE REGION LOOPS

E. Landi[1], M. P. Miralles[2], W. Curdt[3], and H. Hara[4]
[1] Artep, Inc. at Naval Research Laboratory, 4555 Overlook Ave. S.W., 20375-5320, Washington DC, USA
[2] Harvard-Smithsonian Center for Astrophysics, 60 Garden St., MS-50, Cambridge, MA 02138, USA
[3] Max Planck Institut für Sonnensystemforschung, Max Planck Strasse 2, Katlenburg-Lindau 37191, Germany
[4] National Astronomical Observatory of Japan, Osawa, Mitaka, Tokyo 181-8588, Japan
Received 2008 October 22; accepted 2009 January 12; published 2009 March 30

ABSTRACT

In the present work, we use *SOHO*/SUMER, *SOHO*/UVCS, *SOHO*/EIT, *SOHO*/LASCO, *STEREO*/EUVI, and *Hinode*/EIS coordinated observations of an active region (AR 10989) at the west limb taken on 2008 April 8 to study the cooling of coronal loops. The cooling plasma is identified using the intensities of SUMER spectral lines emitted at temperatures in the $4.15 \leqslant \log T \leqslant 5.45$ range. EIS and SUMER spectral observations are used to measure the physical properties of the loops. We found that before cooling took place these loops were filled with coronal hole-like plasma, with temperatures in the $5.6 \leqslant \log T \leqslant 5.9$ range. SUMER spectra also allowed us to determine the plasma temperature, density, emission measure, element abundances, and dynamic status during the cooling process. The ability of EUVI to observe the emitting region from a different direction allowed us to measure the volume of the emitting region and estimate its emission measure. Comparison with values measured from line intensities provided us with an estimate of the filling factor. UVCS observations of the coronal emission above the active region showed no streamer structure associated with AR 10989 at position angles between 242°and 253°. EIT, LASCO, and EUVI-A narrowband images and UVCS spectral observations were used to discriminate between different scenarios and monitor the behavior of the active region in time. The present study provides the first detailed measurements of the physical properties of cooling loops, a very important benchmark for theoretical models of loop cooling and condensation.

Key words: Sun: activity – Sun: corona – Sun: UV radiation

1. INTRODUCTION

Active regions are one of the basic components of the solar corona, and they host the large-scale activity events in the solar atmosphere. Their plasma is highly structured by an all-pervading magnetic field, and they show activity at all scales. One of the building blocks of active regions are magnetic loops that confine hot plasma, insulate it, and include most of the material of the active region itself. The physical properties of active region loops can be very different. They range from hot, fast evolving postflare loops to quiescent active region loops with temperatures in the 1–3 MK range, to transition region loops exhibiting strong dynamic behavior and undergoing rapid changes in their temperature and density. Understanding the physics of active region loops is a crucial step toward the prediction of active region evolution, activity and energetics, as well as toward the understanding of the heating of its plasmas and of the solar corona itself.

Loops with temperatures below 1 MK have been the focus of considerable attention in the past because they undergo significant evolution in relatively short timescales. Cool loops have been known for a long time for their strong dynamics and fast evolution, as well as for depleting their material rapidly. Many studies were carried out to understand their evolution, as for example by Levine & Withbroe (1977). Early observations of dynamics and rapid evolution of cool loops were reviewed by Kjeldseth Moe & Brekke (1998), who also extended such observations to *SOHO*/CDS. However, the rapidity of plasma cooling, and the need of observing several individual spectral lines to carry out plasma diagnostics, has limited the number of studies aimed at measuring the physical properties of cooling plasmas. Nevertheless, cooling processes have attracted growing attention in the recent past.

In fact, for many years loops were regarded as being in static equilibrium and steadily heated. Observations from *Yohkoh*, *SOHO*, and *TRACE* started to challenge this picture. For example, spectral observations from *SOHO*/CDS demonstrated that standard loop models with steady heating are unsuccessful at reproducing the measured temperatures (Landi & Landini 2004). Time-dependent theoretical models of impulsive heating followed by cooling started to attract growing attention, so that cooling has now become a key feature in theoretical and experimental investigations. For example, Schrijver (2001) carried out a quantitative study of cooling coronal loops using the *TRACE* imaging telescope. He concluded that cooling loops were a rather common phenomenon, associated with downward motions of the cooling plasma, leading to loop evacuation. Similar results were obtained by De Groof et al. (2004, 2005) using fast time sequences of images from an EIT shutterless campaign. Several studies have been carried out in the past to understand the evolution of loops in the 1–5 MK range and to correlate loops at different temperatures observed by different instruments. Hot loops were observed using the SXT instrument on board the *Yohkoh* satellite, and several authors tried to correlate them with structures observed at lower temperatures. For example, Schmieder et al. (1996) correlated SXT and H_α observations and found that cool loops were the results of cooling of hot postflare loops, and they also found that the measured cooling time was consistent with estimates using a model improved from Svestka (1987). Several authors tried to investigate the relationship between *Yohkoh* hot loops with cooler loops observed by EIT and *TRACE*, in an attempt to determine whether the latter were the result of the cooling of the former. Nagata et al. (2003) and Schmieder et al. (2004) found that little correlation exist between *Yohkoh* loops on one side, and EIT and *TRACE* loops observed in the EUV on the other.

They also determined that their location and temporal evolution were different. Winebarger & Warren (2005) were successful at correlating a handful of SXT and *TRACE* loops, and showed that their evolution was consistent with an impulsive-heated, multiple-strand cooling loop scenario.

Yohkoh, *TRACE*, and EIT provided excellent spatial and temporal coverage, and permitted great advances in the study of loop physics and evolution. However, their lack of spectral resolution limited their diagnostic capabilities. More recently, O'Shea et al. (2007) used *SOHO*/CDS spectroscopic observations to measure the properties of plasma condensations in coronal loops. They used a sit-and-stare sequence of six lines from ions spanning the 3×10^4 K to 2.5×10^6 K temperature range to observe intensity enhancements at transition region temperatures that corresponded to dimming of coronal lines, and blueshifts corresponding to speeds up to 100 km s^{-1}. They interpreted the intensity changes as the first spectroscopic evidence of plasma condensation taking place in coronal loops. The Doppler shifts they measured indicated downward flows of the cooling material toward the chromosphere. However, the lines available to O'Shea et al. (2007) did not allow them to measure the physical properties of the cooling plasma.

Cooling loops and plasma condensations are very important because their fast evolution and their dynamics can be studied both under the light of coronal heating models as well as of mass transfer to and from the chromosphere and the corona. For example, rapid plasma cooling has also been observed in very moderate flares. Hara et al. (2006) studied rapid cooling of coronal plasma in a very weak flare, observing that the plasma rapidly cooled from coronal to chromospheric temperature using EUV and optical coronal lines formed at around 1×10^6 K. Feldman et al. (2003) used SUMER observations of a C8 flare to follow the light curves of many ions, detecting the onset of very rapid cooling and out-of-equilibrium conditions as the plasma temperature reached $\approx 1 \times 10^6$ K. The similarity between the cooling in these events, and that of larger flares on one side, and of quiescent cool loops on the other, raises the question of whether the cooling mechanisms and evolution are similar.

Cooling loops have also been connected to prominence formation. In fact, there are two main classes of models that address how prominences form, whose main difference is the driving force: pressure-driven models and magnetic field-driven models. The latter mostly rely on the idea that reconnection at photospheric or chromospheric levels uplifts reconnected field lines, who in turn drag frozen-in photospheric and chromospheric material upward (Priest et al. 1996; Galsgaard & Longbottom 1999 and references therein). In other models, reconnection generates jets that replenish loops with chromospheric plasma (Wang 1999).

Pressure-driven models are based on the pile-up of cold material driven into magnetic loops by pressure imbalance at the footpoints. The increasing density enhances radiative losses sufficiently enough to start runaway radiative cooling of coronal material to chromospheric temperatures. These density enhancements are due either to stationary footpoint heating (Karpen et al. 2001, 2003) or to impulsive heating (Karpen & Antiochos 2008). In either case, models predict the recurrent cooling and condensation of loop coronal material, which can either fall down along the loop field lines toward the chromosphere, or remain confined at the initial heights for some time (Karpen et al. 2003). Cooling and condensing loops are considered to be the signature of this scenario, so the measurement of their physical properties is of paramount importance for benchmarking these theoretical models. Pressure-driven models are quite advanced in the sense that they allow the computation of line intensities as a function of time, which can be directly compared with observations.

The aim of the present work is to study the temporal evolution of active region cooling plasma and to measure its physical properties in order to provide experimental benchmarks to theoretical models. We measured the physical properties of rapidly cooling plasma observed in an active region using the SUMER spectrometer on board the *SOHO* satellite determining the temperature, density, emission measure, and element abundances of the cooling material both before and during the cooling process for the first time. *Hinode*/EIS observations are also used to help characterizing the plasma properties before the onset of the cooling. In addition, *SOHO*/UVCS spectral observations, and *SOHO*/EIT, *SOHO*/LASCO, and *STEREO*/EUVI images are used to understand the geometry and evolution of the emitting coronal plasma, as well as discriminating between different evolution scenarios. A comparison of our measurements with theoretical models will be done in a future paper.

The observations are described in Section 2, while the morphology and evolution of the emitting plasma are discussed in Section 3. Plasma diagnostics is carried out in Section 4, and results are discussed and summarized in Section 5.

2. OBSERVATIONS

2.1. SUMER Spectral Scan

On 2008 April 8 we run a "refspec" sequence with SUMER on active region 10989 that had crossed the west limb by 10 UT on the same day. A "refspec" consists of a sit-and-stare spectral scan encompassing the whole SUMER wavelength range. The instrument configuration only allows simultaneous imaging on the detector of a ≈43 Å wide section of the SUMER spectrum, so we divided the entire 660–1500 Å range allowed by SUMER detector B into 37 sections observed consecutively, each with a 300s exposure time and a 20.8 Å offset from the previous section. The entire spectral scan took approximately 3 hr 15 minutes to complete, from April 8 21:08 UT to April 9 00:21 UT. The 4″×300″ slit was used, and its center was pointed at (1000″, −414″). The field of view is shown in Figure 1 in gray superimposed to EIT images in all four channels and to the EIS slit. The top third of the slit (corresponding to pixels 0 to ≃100) crosses the active region. No major activity like flares or coronal mass ejections (CMEs) took place while this sequence was run. For more details about SUMER, see Wilhelm (1995).

All data were cleaned, calibrated, and corrected for geometrical distortion using the standard SUMER software available in the SolarSoft library. The SUMER spectra resulting from this observation presented features typical of moderately active plasma, with the intensity of coronal lines declining rapidly from pixel 150 to 300 as the slit imaged quieter plasma. The absence of lines from highly ionized Fe ions such as Fe XVII 1153.17 Å or Fe XVIII 974.86 Å ensured that the plasma temperature was moderate.

2.2. EIS Spectral Scan

Between April 8 19:30 UT and April 9 05:00 UT *Hinode*/EIS was observing the same region, with its 2″×512″ slit centered at (1000″, −412″). The EIS field of view, shown in Figure 1 in white, included the SUMER one as well as additional 104″

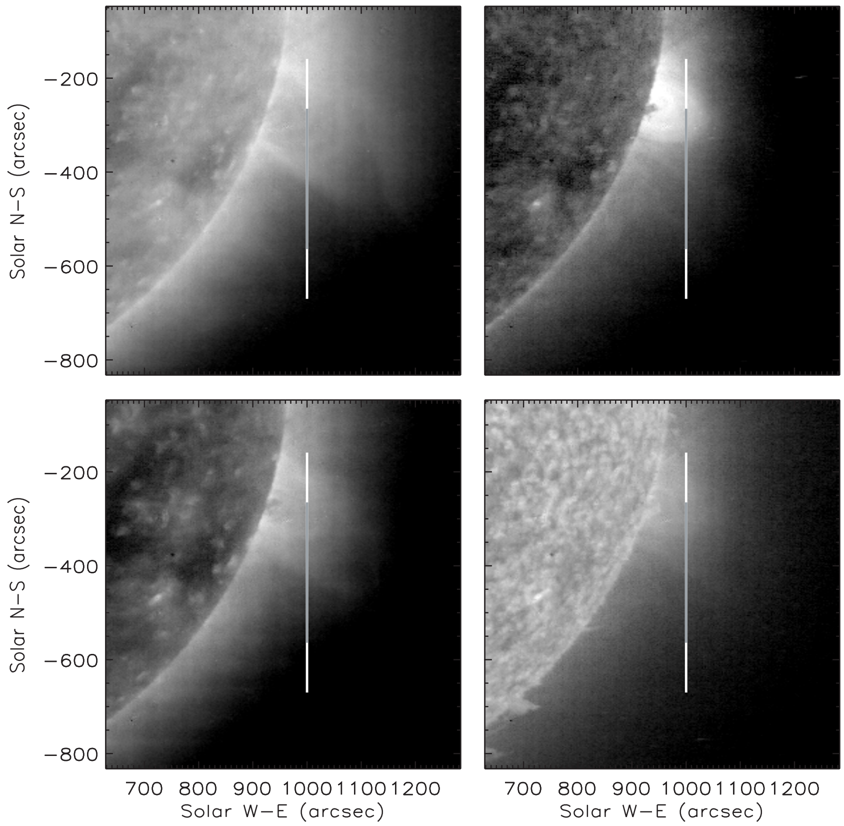

Figure 1. EIT images of active region 10989 at the west limb on April 8 at 7 UT. The EIS slit field of view, 2″×512″ wide and centered at (1000″,−412″), is superimposed to each image as a white line. The SUMER field of view overlaps the EIS one as a gray line. Top left: Fe IX, X 171 Å channel. Top right: Fe XV 284 Å channel. Bottom left: Fe XII 195 Å channel. Bottom right: He II 304 Å channel.

and 108″ at the north and south edges of the SUMER slit, respectively. The entire EIS spectral range was recorded in a sit-and-stare mode with a cadence of 600 s for each exposure. This sequence was run continuously, but problems in the telemetry rate and data gaps have limited the amount of data being successfully transmitted to the ground. In particular, data were available to us only in the following time intervals: 19:30-20:00 UT, 21:00-21:30 UT, 22:30-23:00 UT, 00:00-00:30 UT, 01:30-02:00 UT, 03:00:03:30 UT, and 04:30-05:00 UT. A description of the EIS instrument can be found in Culhane et al. (2007).

The data were not in the standard FITS format and the EIS preparation routines available in SolarSoft could not be applied. We have done the basic data reduction applying individual routines to the raw data. We first de-biased the data, and then we developed a routine to remove both cosmic rays and warm and hot pixels. This procedure first recognizes the presence of a warm or hot pixel by comparing the intensity of each pixel to the median of the intensity of the nearest-neighbor pixels. Pixels with values larger than four times the median value were flagged to build an empirical map of the warm and hot pixels. This procedure also flagged most cosmic rays: the long exposure time of each EIS data set ensured that a large number of them where present in the field of view. The intensity of the flagged pixels was replaced with the median of the intensity of the nearest neighbors. A similar procedure was then applied to the residual cosmic rays by considering the values of each pixel along the EIS time series of observations. Pixels whose intensity was larger than four times the median of all EIS observations were replaced with the median of the intensity of the nearest neighbor pixels in the same frame. The threshold detection value of 4 used for both cosmic rays and warm and hot pixels was selected by trial and error, in a compromise between the effort of eliminating all "bad" pixels, and the need for sparing bright pixels due to real solar emission.

We ended up with a series of full images of the entire EIS spectrum in counts s^{-1}. Line intensities were determined summing all counts under the line profiles, and subtracting the background. Results were converted into physical units using the intensity calibration of Brown et al. (2008).

2.3. SUMER and EIS Alignment and Relative Intensity Calibration

The SUMER and EIS slits were centered nominally at the same coordinates, so that in principle the SUMER field of view was included in the EIS one. Small shifts of the relative pointing along the east–west direction (e.g., of a few arcseconds) are very difficult to detect, even if the active region is observed outside the disk and its structure is relatively simple. Such shifts, however, may cause significant effects on plasma diagnostics when studying individual structures, while they can be ignored when larger structures are considered since the change in the large-scale physical properties of solar plasmas are moderate within a few arcseconds. In the present work, we are concerned with one initially quiescent, extended source and with one very localized, highly transient source. The EIS data set includes only the former target, so the effects of any east–west offset are expected to be limited. However, in order to minimize uncertainties, we use EIS results, when available, only to confirm those obtained with SUMER.

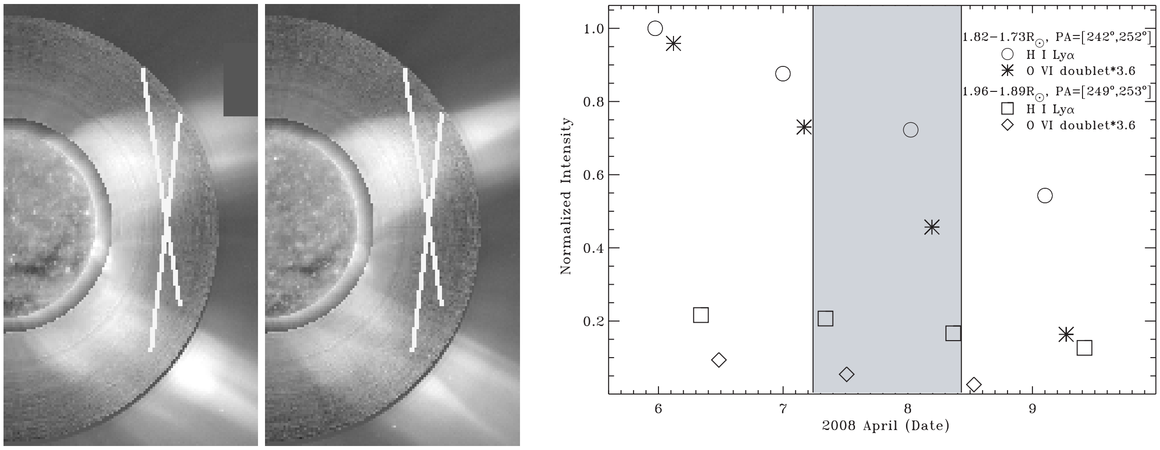

Figure 2. Left: UVCS slit positions projected on the plane of the sky for 2008 April 7 (18:50 UT) and 8 (17:26 UT) shown on the composite image of *SOHO*/EIT 195 Å (innermost image), the ground-based Manua Loa Solar Observatory/HAO Mark IV (middle image) and the *SOHO*/LASCO C2 (outermost image) coronagraphs (see Section 2.4, 3). Right: UVCS normalized intensities of H I Lyα λ1215.67 (circles and squares) and O VI doublet $\lambda\lambda$1031.91, 1037.61 (stars and diamonds) for 2008 April 6–9. The gray area shows the times when AR 10989 was on the plane of the sky. The O VI data were multiplied by a factor of 3.6 to plot them on the same scale as the H I Lyα data.

The relative position of SUMER and EIS slits along the north–south direction can, in contrast, be determined by looking at the intensity distribution along the slit of lines emitted by the same ion, at the same time in spectral ranges of both instruments. First, we corrected the EIS data for the spatial displacement of the EIS images due to the tilt of the grating and the offset between the two EIS channels. We then used lines from Fe VIII and Si VII to determine the relative position of the EIS and SUMER field of view by finding the shift of the SUMER slit in the EIS field of view that minimized the differences between the intensity profiles of the Fe VIII 185.60 Å and 721.26 Å lines, and of the Si VII 275.35 Å and 1049.20 Å lines. We found that the SUMER slit was placed 7″ southward of the nominal position relative to the EIS one. We took this displacement into account to coalign the two observations in the north–south direction.

The relative intensity calibration of the two spectrometers is of great importance when intensities measured with both instruments are compared. Both EIS and SUMER have been calibrated on the ground, and their calibrations have been monitored in time. Nevertheless, it is important to check that their relative calibration is accurate. Since the wavelength ranges of the two instruments do not overlap, it is necessary to use the solar spectrum to check their relative calibration. Muglach et al. (2009) performed such a task by using off-disk long exposure observations of the unstructured quiet Sun, and showed that the cross-calibration of the two instruments was accurate within experimental uncertainties.

2.4. *UVCS Observations*

UVCS observations of this active region were made continuously during 2008 April 6–9. The slit was positioned at a heliocentric height of 1.7 $R_\odot$ at the west limb (P.A. = 263°, 279° in the radial direction normal to the slit). The data reported here were taken with the O VI channel. The instrument configuration for the observations included an entrance slit of 50 μm, a spatial binning of 4 pixels (28 ″) for H I Lyα λ1215.67 and 8 pixels (56″) for O VI doublet $\lambda\lambda$1031.93, 1037.62, a spectral binning of 1 pixel (0.0915 and 0.0993 Å, respectively), and an instantaneous field of view of 40′ × 14″. For a description of the UVCS instrument, see Kohl et al. (1995, 2006). Details concerning the analysis of UVCS data are given by Gardner et al. (1996, 2000, 2002) and Kohl et al. (1997, 1999). The UVCS Data Analysis Software (DAS) was used to remove image distortion and to calibrate the data in wavelength and intensity. Figure 2 shows the position of the UVCS slit as projected in the plane of the sky, superimposed on a composite image from *SOHO*/EIT, the Manua Loa Solar Observatory/HAO Mark IV and the *SOHO*/LASCO C2 coronagraphs for the April 7 and 8 observations.

3. MORPHOLOGY AND EVOLUTION

AR 10989 was the last of a group of three active regions moving toward the west limb in Carrington Rotation 2068 during the International Heliophysical Year's (IHY) Whole Heliospheric Interval campaign. This active region was followed by a large low-latitude coronal hole. The active region reached the west limb on approximately April 7 at 6 UT and went behind the plane of the sky by April 8 at 10 UT. We can see that there is not apparent white-light emission in the corona at the west limb associated with the active region above 1.3 $R_\odot$ (Figure 2). Nevertheless, we examined the spatial distribution of the line intensities along the UVCS slit, and in time, and extracted four regions in the corona covering an extent of ∼70″ (which corresponds to a P.A. range of 242°–253°) around the location of the active region. Figure 2 also shows the corresponding normalized UVCS line intensities for H I Lyα and O VI doublet for those locations during April 6–9. The O VI data, from the contribution of both lines in the doublet, were multiplied by a factor of 3.6 to plot them on the same intensity scale as the H I Lyα data. The data for each species taken in the same day were grouped in two time periods corresponding to each slit position. This resulted in two intensity data points for each species per day in Figure 2. The intensity of both ions, H I Lyα and O VI doublet, shows a decreasing pattern from April 6, when the end-edge of the active region ahead of AR 10989 was in the line of sight. There is no intensity peak consistent with the time when the active region was right at the limb, that is, when most line intensities should have reached maximum. A low-density coronal structure at a lower P.A. may have existed, but the bright southwestern streamer belt next to it could have hidden it from our line of sight. *STEREO*/COR 1 and COR 2 images also did not show any indication for an extended coronal structure in addition to the background streamer belt. This reinforces the idea

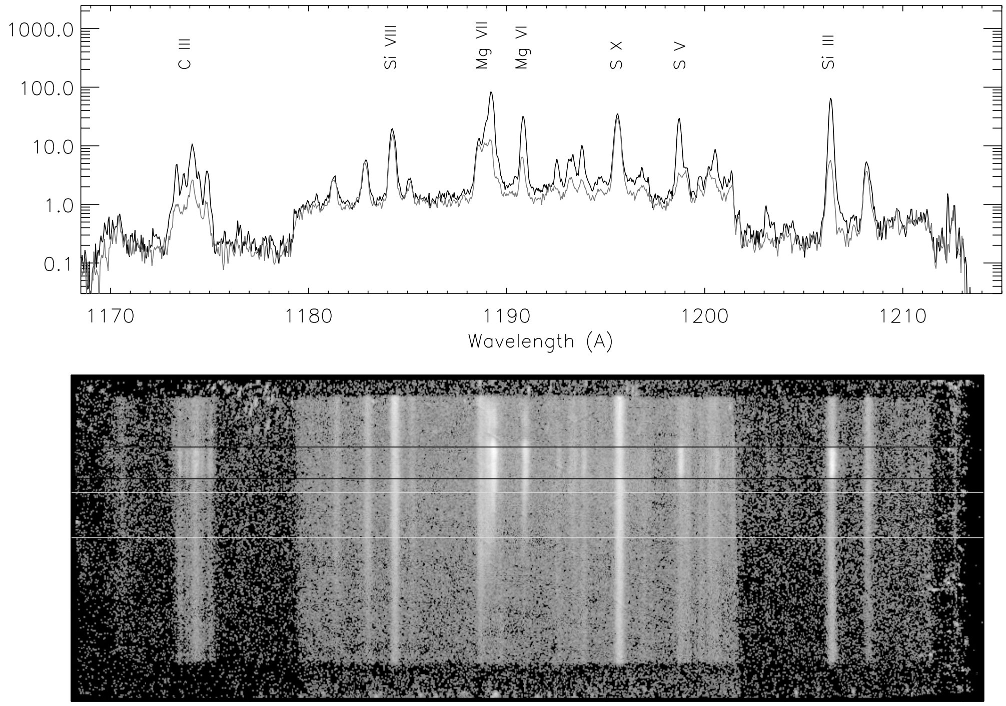

Figure 3. SUMER spectrum in the 1169–1213 Å range. Images of the SUMER detector, reversed so that north is up and south is down, are shown at the bottom. White and black horizontal lines mark the portions of the slit used to average the spectrum displayed in the top panel: black lines correspond to the black spectrum; white lines to the gray spectrum.

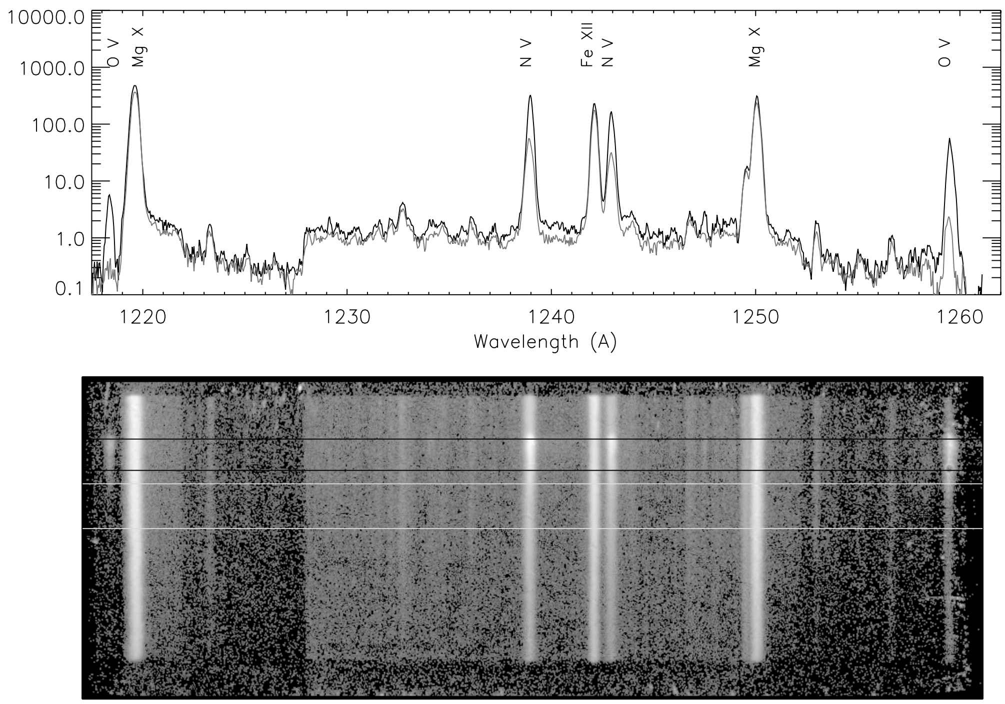

Figure 4. SUMER spectrum in the 1218–1260 Å range. Images of the SUMER detector, reversed so that north is up and south is down, are shown at the bottom. White and black horizontal lines mark the portions of the slit used to average the spectrum displayed in the top panel: black lines correspond to the black spectrum; white lines to the gray spectrum.

that there seems to be no coronal streamer structure associated with the active region at position angle 242°–253°, and that the emission seen at 1.3 $R_\odot$ in the white-light images corresponds to the top of the active region loops.

Since SUMER spectra also observed continuously the emitting region, we have inspected them in order to understand the evolution of the active region below 1.3 $R_\odot$. There are two peculiar features in the SUMER spectra that will be the focus of the present work. Two 43 Å wide sections of the spectrum are displayed in Figures 3 and 4. Coronal lines such as Si VIII 1183.99 Å, S X 1196.22 Å, Mg X 609.79 Å, and 624.94 Å at second order, and Fe XII 1242.01 Å have very uniform images, with a very smooth and continuous intensity distribution along the slit direction (the Y-axis in Figures 3 and 4). In contrast, colder ions such as C III, Si III, S V, O V, Mg VI, VII, and N V have very different intensity distributions with an enhancement (marked by black horizontal lines) in the north section of the slit, inside the active region. This enhancement changes in different ions and at different times.

Figure 3 shows that the Mg VI intensity distribution is more elongated than that of the colder emission from C III, Si III, S V, O V, and N V ions. Once the scattered light contribution has been removed from the latter lines, the emission in these colder ions is much more localized. We have inspected the entire SUMER wavelength range for such features and found that indeed all ions with formation temperature in the $5.6 < \log T < 5.9$ observed before 22:50 UT share the same elongated shape as Mg VI. These ions and their observed lines are listed in Table 1, along with their temperature of maximum abundance $\log T_{\rm max}$. Examples of the normalized intensity distribution of these ions along the slit are given in Figure 5 as a function of time. Their intensity distribution is fairly constant with time, until a decrease in intensity around pixels 30–50 is visible after 22:50 UT. After 23:13 UT this structure seems to disappear and the intensity distribution of lines formed in the $5.6 \leqslant \log T \leqslant 5.9$ becomes the same as that of the coronal lines. An example is given in Figure 6, where the normalized intensity profiles of two Ca IX lines (emitted at $\log T \approx 5.8$) is compared to that of the Mg IX 706.06 Å coronal line, emitted at $\log T \approx 6.0$. The two Ca IX lines were observed at 21:40 UT (left) and 23:55 UT (right): their intensity profile is completely different. This suggests that at 21:40 UT Ca IX was mostly emitted by a different plasma than Mg IX, while at 23:55 UT that plasma has disappeared, and only the background coronal plasma, that also emits the Mg IX line, contributes to the Ca IX line intensity. EIS lines formed in the $5.6 \leqslant \log T \leqslant 5.9$ range show the same behavior. However, after April 9 00:20 UT EIS line intensities show that this plasma starts to reform and to have a shape similar to the one it had before 22:50 UT. We will refer to the plasma emitting the ions listed in Table 1 as the "hot feature" (HF).

Table 2 lists all the ions showing a more localized emission than HF ions. Their intensities share three peculiar features. First, they are only observed between 22:52 UT and 23:35 UT. Second, their intensity distribution along the slit evolves during those 40 minutes. Third, all these ions are colder than those in the HF, and their temperature of formation is in the $4.15 \leqslant \log T \leqslant 5.45$ range. Figures 7–9 show the normalized intensity distribution of these ions along the slit. The first signature of this plasma feature occurs at 22:52 UT with O IV and it is very localized at pixels 30–40, corresponding to the dip of intensity in HF emission at 22:57 UT shown in Figure 5. In the subsequent SUMER frames between 23:05 UT and 23:13 UT this feature broadens, moves northward, and eventually concentrates in a sharp peak between pixels 50-60 at 23:19 UT. This last peak moves northward up to pixel 30-40 at 23:35 UT and then it disappears. No more emission from these cold lines, occurring at wavelengths observed after 23:35 UT, were observed. EIS data were taken only until 23:00 UT and do not show any of the lines of ions such as those listed in Table 2, even though the observation between 22:50 UT and 23:00 UT might have shown O IV and O V. We will refer to this feature as the "cold feature" (CF).

Figures 10 and 11 display the emission of the HF and CF, respectively, as a function of time from the beginning of the SUMER spectral scan until 23:40 UT. These images were constructed by placing many slit images side by side, that were obtained in the following way. Adjacent slit images were taken from two subsequent SUMER spectral frames, so that each frame included a different wavelength range. Within each frame, the slit image was determined by measuring the intensity of a line emitted by the HF (for Figure 10) and CF (for Figure 11), subtracting the background and scattered light contribution, and normalizing the result. Figures 10 and 11 are built by placing side by side images of this kind taken in consecutive frames, so that the Y-axis represents the position along the slit, while the X-axis represents time (UT hours).

Figures 10 and 11 are remarkably different. The HF is fairly stable in time until 22:50 UT as far as position and size are concerned, although the peak of the emission slowly

Table 1
SUMER Lines Emitted by the HF, Visible Until 23:13 UT

Time (UT)	Ion	Wvl. (Å)	Transition	$\log T_{\rm max}$
21:08	Fe VIII	697.16	$3p^64p\ ^2P_{1/2}$ - $3p^64d\ ^2D_{3/2}$	5.56
21:13	Fe VIII	697.16	$3p^64p\ ^2P_{1/2}$ - $3p^64d\ ^2D_{3/2}$	5.56
21:13	Fe VIII	721.26	$3p^64p\ ^2P_{3/2}$ - $3p^64d\ ^2D_{5/2}$	5.56
21:18	Fe VIII	721.26	$3p^64p\ ^2P_{3/2}$ - $3p^64d\ ^2D_{5/2}$	5.56
21:23	Mg VIII	762.66	$2s^22p\ ^2P_{1/2}$ - $2s2p^2\ ^4P_{3/2}$	5.90
21:23	Mg VIII	772.26	$2s^22p\ ^2P_{3/2}$ - $2s2p^2\ ^4P_{5/2}$	5.90
21:28	Mg VIII	762.66	$2s^22p\ ^2P_{1/2}$ - $2s2p^2\ ^4P_{3/2}$	5.90
21:28	Mg VIII	772.26	$2s^22p\ ^2P_{3/2}$ - $2s2p^2\ ^4P_{5/2}$	5.90
21:28	Mg VIII	782.36	$2s^22p\ ^2P_{3/2}$ - $2s2p^2\ ^4P_{3/2}$	5.90
21:28	Mg VIII	789.41	$2s^22p\ ^2P_{3/2}$ - $2s2p^2\ ^4P_{1/2}$	5.90
21:34	Mg VIII	782.36	$2s^22p\ ^2P_{3/2}$ - $2s2p^2\ ^4P_{3/2}$	5.90
21:34	Mg VIII	789.41	$2s^22p\ ^2P_{3/2}$ - $2s2p^2\ ^4P_{1/2}$	5.90
21:39	Ca IX	821.27	$3s3p\ ^1P_1$ - $3p^2\ ^1D_2$	5.80
21:44	Ca IX	821.27	$3s3p\ ^1P_1$ - $3p^2\ ^1D_2$	5.80
21:44	Mg VII	854.72	$2s^22p^2\ ^3P_1$ - $2s2p^3\ ^5S_2$	5.80
21:49	Mg VII	854.72	$2s^22p^2\ ^3P_1$ - $2s2p^3\ ^5S_2$	5.80
21:49	Mg VII	868.19	$2s^22p^2\ ^3P_2$ - $2s2p^3\ ^5S_2$	5.80
21:54	Mg VII	868.19	$2s^22p^2\ ^3P_2$ - $2s2p^3\ ^5S_2$	5.80
21:54	Ne VII	895.17	$2s^2\ ^1S_0$ - $2s2p\ ^3P_1$	5.71
22:00	Ne VII	895.17	$2s^2\ ^1S_0$ - $2s2p\ ^3P_1$	5.71
22:05	S VI	933.38	$3s\ ^2S_{1/2}$ - $3p\ ^2P_{3/2}$	5.29
22:10	S VI	933.38	$3s\ ^2S_{1/2}$ - $3p\ ^2P_{3/2}$	5.29
22:15	Ne VII	973.33	$2s2p\ ^1P_1$ - $2p^2\ ^1D_2$	5.71
22:20	Ne VII	973.33	$2s2p\ ^1P_1$ - $2p^2\ ^1D_2$	5.71
22:20	Ne VI	997.03	$2s^22p\ ^2P_{1/2}$ - $2s2p^2\ ^4P_{1/2}$	5.61
22:20	Ne VI	999.18	$2s^22p\ ^2P_{3/2}$ - $2s2p^2\ ^4P_{5/2}$	5.61
22:26	Ne VI	999.18	$2s^22p\ ^2P_{3/2}$ - $2s2p^2\ ^4P_{5/2}$	5.61
22:26	Ne VI	1005.69	$2s^22p\ ^2P_{3/2}$ - $2s2p^2\ ^4P_{3/2}$	5.61
22:26	Ne VI	1010.21	$2s^22p\ ^2P_{3/2}$ - $2s2p^2\ ^4P_{1/2}$	5.61
22:31	Ne VI	1005.69	$2s^22p\ ^2P_{3/2}$ - $2s2p^2\ ^4P_{3/2}$	5.61
22:31	Ne VI	1010.21	$2s^22p\ ^2P_{3/2}$ - $2s2p^2\ ^4P_{1/2}$	5.61
22:36	Si VII	1049.20	$2s^22p^4\ ^3P_1$ - $2s^22p^4\ ^1S_0$	5.76
22:36	Al VII	1053.99	$2s^22p^3\ ^4S_{3/2}$ - $2s^22p^3\ ^2P_{3/2}$	5.80
22:36	Al VII	1056.92	$2s^22p^3\ ^4S_{3/2}$ - $2s^22p^3\ ^2P_{1/2}$	5.80
22:41	Si VII	1049.20	$2s^22p^4\ ^3P_1$ - $2s^22p^4\ ^1S_0$	5.76
22:41	Al VII	1053.99	$2s^22p^3\ ^4S_{3/2}$ - $2s^22p^3\ ^2P_{3/2}$	5.80
22:41	Al VII	1056.92	$2s^22p^3\ ^4S_{3/2}$ - $2s^22p^3\ ^2P_{1/2}$	5.80
22:52	Ne VI	558.69	$2s^22p\ ^2P_{1/2}$ - $2s2p^2\ ^2D_{3/2}$	5.80
22:52	Ne VII	559.95	$2s2p\ ^3P_0$ - $2p^2\ ^3P_1$	5.71
22:52	Ne VII	561.73	$2s2p\ ^3P_2$ - $2p^2\ ^3P_2$	5.71
22:52	Ne VI	562.70	$2s^22p\ ^2P_{3/2}$ - $2s2p^2\ ^2D_{5/2}$	5.61
		562.80	$2s^22p\ ^2P_{3/2}$ - $2s2p^2\ ^2D_{3/2}$	
22:57	Ne VI	558.69	$2s^22p\ ^2P_{1/2}$ - $2s2p^2\ ^2D_{3/2}$	5.61
22:57	Ne VII	559.95	$2s2p\ ^3P_0$ - $2p^2\ ^3P_1$	5.71
22:57	Ne VII	561.73	$2s2p\ ^3P_2$ - $2p^2\ ^3P_2$	5.71
22:57	Ne VI	562.70	$2s^22p\ ^2P_{3/2}$ - $2s2p^2\ ^2D_{5/2}$	5.61
		562.80	$2s^22p\ ^2P_{3/2}$ - $2s2p^2\ ^2D_{3/2}$	
23:02	Ca VIII	582.83	$3s^23p\ ^2P_{1/2}$ - $3s3p^2\ ^2D_{3/2}$	5.75
23:07	Ca VIII	582.83	$3s^23p\ ^2P_{1/2}$ - $3s3p^2\ ^2D_{3/2}$	5.75
23:07	Ar VII	585.76	$3s^2\ ^1S_0$ - $3s3p\ ^1P_1$	5.53
23:13	Mg VI	1190.12	$2s^22p^3\ ^4S_{3/2}$ - $2s^22p^3\ ^2P_{3/2}$	5.64
23:13	Mg VI	1191.67	$2s^22p^3\ ^4S_{3/2}$ - $2s^22p^3\ ^2P_{1/2}$	5.64

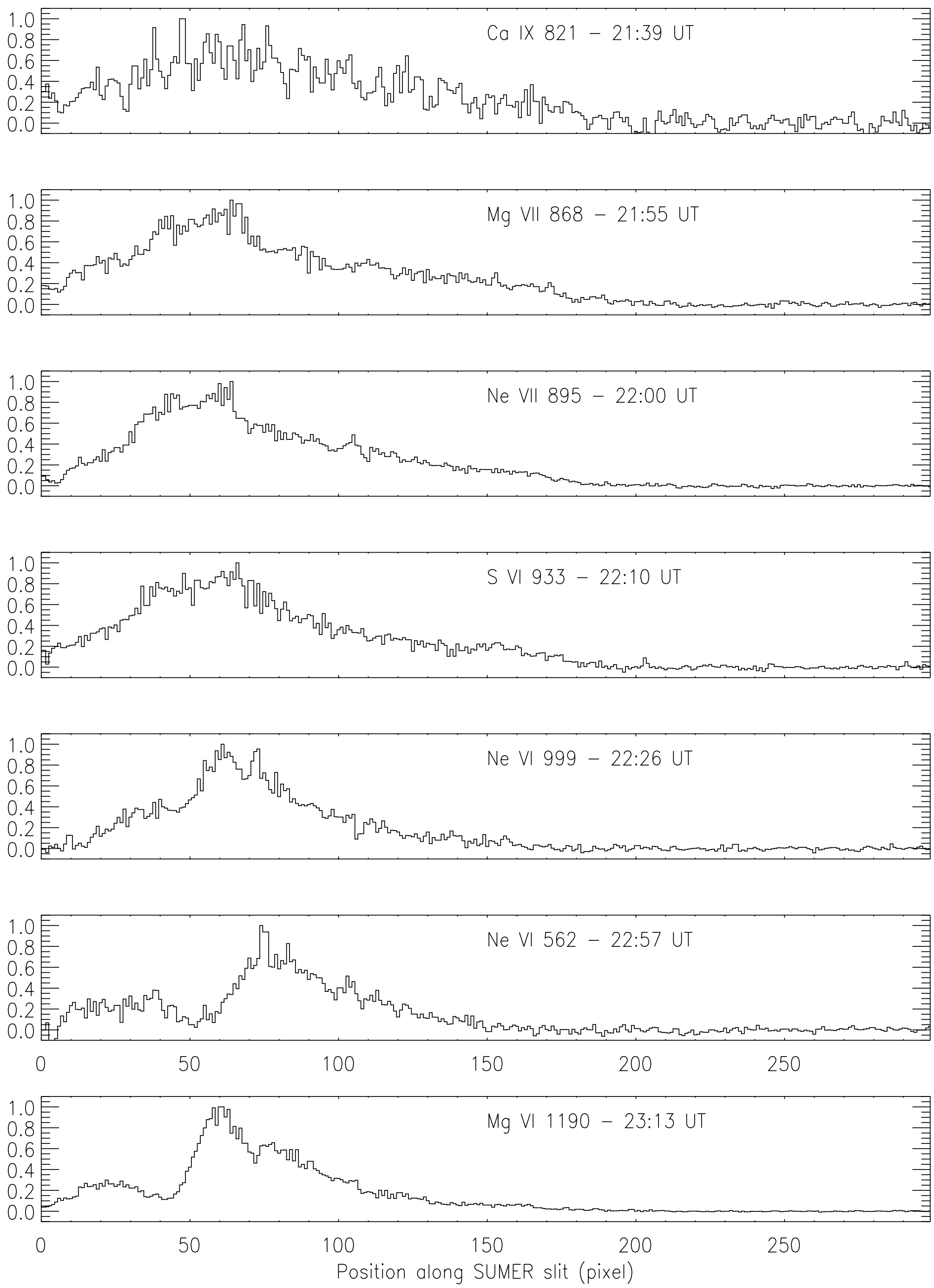

Figure 5. Intensity profiles of lines emitted by the HF versus SUMER pixel position. Pixels 0 and 300 correspond to the north and south edges of the slit, respectively.

shifts between pixels 220 and 240 during the first 1.5 hr of observation. At around 22:50 UT the emission around pixels 230–250 suddenly drops, and at the same time and location, the first signature of the CF becomes visible. Signatures of the HF are still observed until 23:13 UT, and they are cospatial to those of the CF. It is to be noted that HF lines after 23:00 UT are emitted by Mg VI only. Their emission, shown in Figure 5 (bottom panel), resembles in part that of CF lines observed at the same time. We have associated Mg VI with the HF somewhat arbitrarily, because of its formation temperature, but it is likely that the intensity of this ion is partly or even completely emitted by the CF at these locations. After the brightenings at 22:50 UT and 23:00 UT, the HF disappears, and the intensity distribution along the slit of lines formed in the $5.6 \leqslant \log T \leqslant 5.9$ becomes the same as for the coronal lines, as shown in Figure 6.

The CF, in contrast, is much more localized, and moves along the slit by $\simeq$40 pixels in 40 minutes approximately, corresponding to an average speed in the plane of the sky of $\simeq$12 km s^{-1}. Its size changes considerably, and narrows toward the end of the life of this feature. No more signature of ions formed at the same temperature as those emitting the CF lines are found after 23:35 UT.

3.1. *Nature of the HF*

The question arises as to the nature of these two features. The behavior of the HF is very stable until 22:50 UT, since the

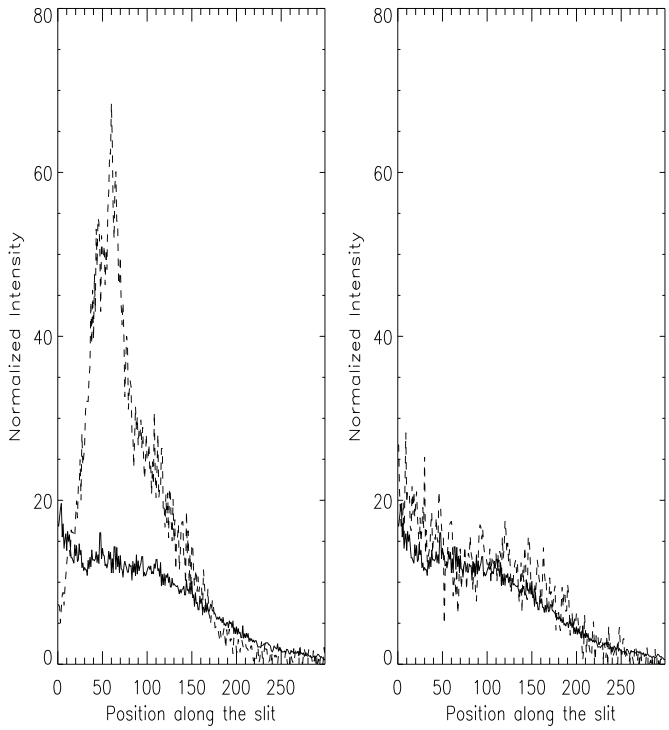

Figure 6. Normalized intensity profiles of the Mg IX 706.06 Å coronal line (full line) and of the Ca IX 821.27 Å (left) and 691.21 Å lines (right), both as dashed lines. The intensities in the left panel were recorded before April 8 21:40 UT; those in the right panel at around April 8 23:55 UT, after the disappearance of the colder material. Pixels 0 and 300 correspond to the north and south edges of the slit, respectively.

intensity distribution of the lines that it emits is essentially the same until then. This leads us to speculate that this ≈ 100″–150″ wide region is actually a stable component of the active region. Since it is observed in ions emitting in the $5.6 \leqslant \log T \leqslant 5.9$ range, its temperature is lower than typical active region values. In principle this region could either be a cold component of the active region (such as the coronal hole-like component identified in other active regions by Landi & Feldman 2008), or the signature of overlying coronal hole plasma in front of the active region, corresponding to the equatorial hole visible in the solar disk behind the active region (Miralles 2008).

However, the rather sudden disappearance of the emission of this plasma, the simultaneous rise of colder emission at the same time and at the same location, and the shape of the EUVI darkening feature in Figure 12, are more compatible with a local event confined into plasma structures within the active region, rather than with the sudden disappearance of an entire large-scale structure such as an equatorial coronal hole. We will further elaborate on this in Section 4.

3.2. Nature of the CF

The transient nature of the CF could be due to a variety of different scenarios: an erupting filament that generates a CME sweeping through the SUMER and EIS slits; an activated prominence or a cool loop that rises above the location of the spectrometers' field of view; or the sudden condensation of local plasma already present in the field of view.

We have used *SOHO*/LASCO and *STEREO*/EUVI-A series of images and UVCS data to help discriminate between these different scenarios. The active region in the SUMER and EIS fields of view had already gone behind the west limb as seen

Table 2
SUMER Lines Emitted by the CF, Visible Between 22:52 UT and 23:35 UT

Time (UT)	Ion	Wvl. (Å)	Transition	$\log T_{\rm max}$
22:52	O IV	553.33	$2s^22p\ ^2P_{1/2}$ - $2s2p^2\ ^2P_{3/2}$	5.18
22:52	O IV	554.08	$2s^22p\ ^2P_{1/2}$ - $2s2p^2\ ^2P_{1/2}$	5.18
22:52	O IV	554.51	$2s^22p\ ^2P_{3/2}$ - $2s2p^2\ ^2P_{3/2}$	5.18
22:52	O IV	555.26	$2s^22p\ ^2P_{3/2}$ - $2s2p^2\ ^2P_{1/2}$	5.18
22:52	Si III	1113.18	$3s3p\ ^3P_2$ - $3s3d\ ^3D_1$	4.68
		1113.21	$3s3p\ ^3P_2$ - $3s3d\ ^3D_2$	
		1113.23	$3s3p\ ^3P_2$ - $3s3d\ ^3D_3$	
22:57	Ne V	572.34	$2s^22p^2\ ^3P_2$ - $2s2p^3\ ^3D_3$	5.46
22:57	Ne V	1145.60	$2s^22p^2\ ^3P_2$ - $2s2p^3\ ^5S_2$	5.46
23:02	Ne V	569.76	$2s^22p^2\ ^3P_1$ - $2s2p^3\ ^3D_1$	5.46
		569.84	$2s^22p^2\ ^3P_1$ - $2s2p^3\ ^3D_2$	
23:02	Ne V	572.34	$2s^22p^2\ ^3P_2$ - $2s2p^3\ ^3D_3$	5.46
23:02	Ne V	1145.60	$2s^22p^2\ ^3P_2$ - $2s2p^3\ ^5S_2$	5.46
23:08	He I	584.34	$1s^2\ ^1S_0$ - $1s2p\ ^1P_1$	4.15
23:08	C III	1174.88	$2s2p\ ^3P_1$ - $2p^2\ ^3P_2$	4.84
23:08	C III	1175.24	$2s2p\ ^3P_0$ - $2p^2\ ^3P_1$	4.84
23:08	C III	1175.59	$2s2p\ ^3P_1$ - $2p^2\ ^3P_1$	4.84
		1175.74	$2s2p\ ^3P_2$ - $2p^2\ ^3P_2$	
23:08	C III	1175.98	$2s2p\ ^3P_1$ - $2p^2\ ^3P_0$	4.84
23:13	C III	1174.88	$2s2p\ ^3P_1$ - $2p^2\ ^3P_2$	4.84
23:13	C III	1175.24	$2s2p\ ^3P_0$ - $2p^2\ ^3P_1$	4.84
23:13	C III	1175.59	$2s2p\ ^3P_1$ - $2p^2\ ^3P_1$	4.84
		1175.74	$2s2p\ ^3P_2$ - $2p^2\ ^3P_2$	
23:13	C III	1175.98	$2s2p\ ^3P_1$ - $2p^2\ ^3P_0$	4.84
23:13	Si II	1193.29	$3s^23p\ ^2P_{1/2}$ - $3s3p^2\ ^2P_{1/2}$	4.13
23:13	Si II	1194.50	$3s^23p\ ^2P_{3/2}$ - $3s3p^2\ ^2P_{3/2}$	4.13
23:13	S V	1199.14	$3s^2\ ^1S_0$ - $3s3p\ ^3P_1$	5.19
23:13	Si III	1206.50	$3s^2\ ^1S_0$ - $3s3p\ ^1P_1$	4.68
23:19	O V	1218.34	$2s^2\ ^1S_0$ - $2s2p\ ^3P_1$	5.37
23:19	N V	1238.82	$2s\ ^2S_{1/2}$ - $2p\ ^2P_{3/2}$	5.26
23:19	N V	1242.81	$2s\ ^2S_{1/2}$ - $2p\ ^2P_{1/2}$	5.26
23:24	N V	1238.82	$2s\ ^2S_{1/2}$ - $2p\ ^2P_{3/2}$	5.26
23:24	N V	1242.81	$2s\ ^2S_{1/2}$ - $2p\ ^2P_{1/2}$	5.26
23:24	O V	629.73	$2s^2\ ^1S_0$ - $2s2p\ ^1P_1$	5.37
23:24	Si II	1260.42	$3s^23p\ ^2P_{1/2}$ - $3s^23d\ ^2D_{3/2}$	4.13
23:24	Si II	1264.74	$3s^23p\ ^2P_{1/2}$ - $3s^23d\ ^2D_{5/2}$	4.13
23:29	O V	629.73	$2s^2\ ^1S_0$ - $2s2p\ ^1P_1$	5.37
23:35	Si III	1294.55	$3s3p\ ^3P_1$ - $3p^2\ ^3P_2$	4.68
23:35	Si III	1298.89	$3s3p\ ^3P_1$ - $3p^2\ ^3P_1$	4.68
		1298.95	$3s3p\ ^3P_2$ - $3p^2\ ^3P_2$	
23:35	Si III	1303.32	$3s3p\ ^3P_2$ - $3p^2\ ^3P_1$	4.68
23:35	Si II	1309.28	$3s^23p\ ^2P_{3/2}$ - $3s3p^2\ ^2S_{1/2}$	4.13

from the Earth's direction, so that the EUVI-B instrument could not be used. *SOHO*/EIT could be used to monitor the properties and activity of the active region at low heights only until the day before the SUMER spectral scan. In order to compare the SUMER slit data to EUVI-A images, we determined the field of view intercepted by the SUMER line of sight in the EUVI-A plane of the sky at the range of longitudes of the active region hosting both HF and CF. This was done by estimating the size of the base of the active region from EIT images of April 5 to be 50″, and assuming that the region hosting the HF and CF was located radially above it. We used the solar rotation rate to calculate the position of the base of the active region at the time of our observation and from geometrical considerations we determined the SUMER field of view in the EUVI plane of the sky. The result is displayed in Figure 12, where it is superimposed to nearly simultaneous images in the EUVI-A 171 Å and 304 Å channels. Note that only the northern half of the SUMER slit field of view is shown.

The erupting CME scenario can be safely discarded, as LASCO movies show that no CME was observed at around

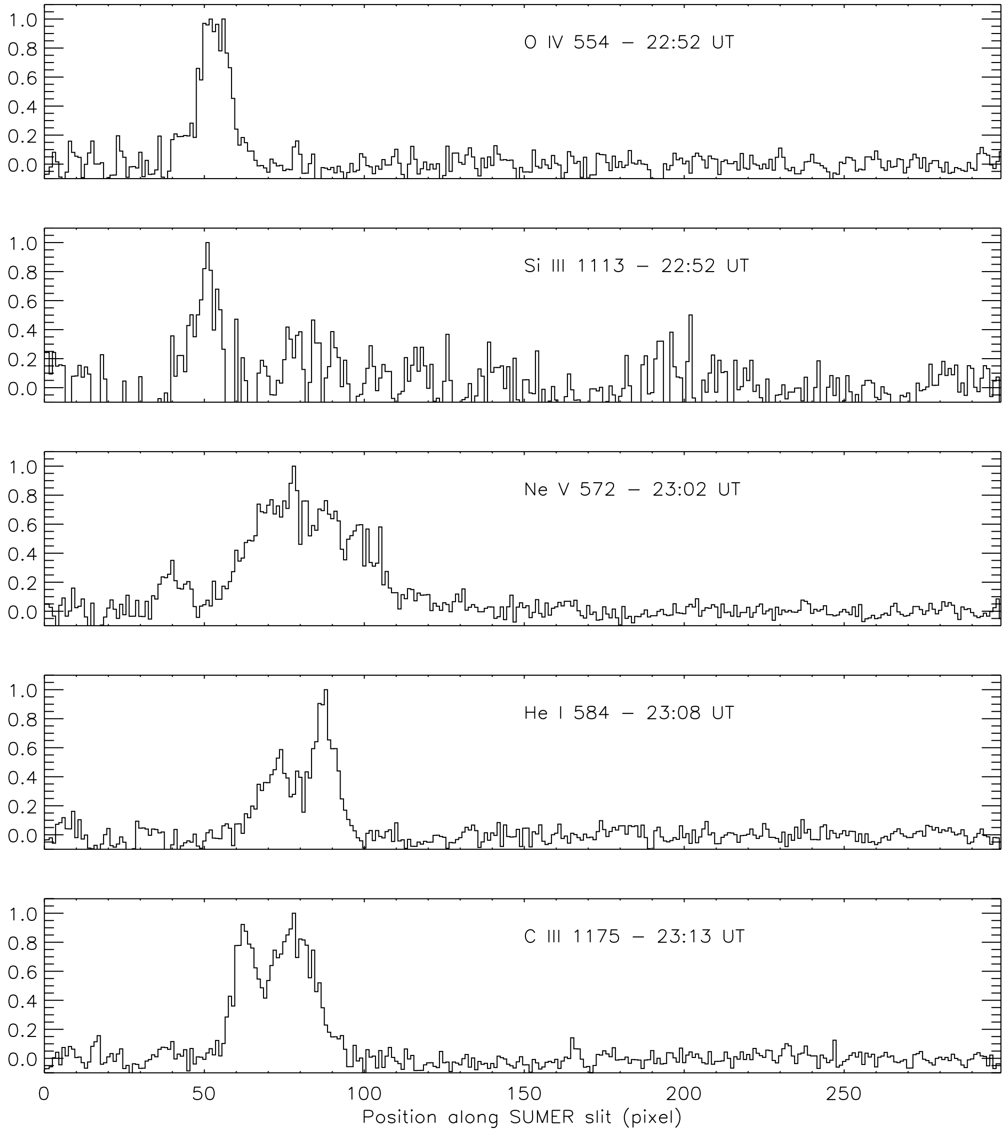

Figure 7. Intensity profiles of lines emitted by the CF versus SUMER pixel position. Pixels 0 and 300 correspond to the north and south edges of the slit, respectively.

22:50-23:30 UT. A weak CME was observed entering the LASCO field of view at around 17:50 UT the same day, and until the day after nothing else happened. The inspection of the EUVI movies in all four channels also showed that no CME was ejected between 22:50 UT and 23:30 UT. This was also confirmed by the UVCS data which did not show any CME front passing through the slit during the cooling event.

The activated prominence scenario was suggested by the presence of a filament in the active region we are considering. This filament was observed in EIT and EUVI images of the active region for many days before April 8. We have inspected the EUVI images in the 304 Å filter to check whether this filament rose to the SUMER height during the present observations. The 10 minute cadence available for the 304 Å filter images did not allow us to finely sample the behavior of the chromospheric plasma at small temporal scales, but it was sufficient to determine that the filament in the active region did not rise to the SUMER heights and hence could not be the source of the CF.

The EUVI 171 Å images were observed with a 2.5 minute cadence and could be used to understand whether some activity could be correlated with the evolution of the CF. The 171 Å filter is moderately sensitive to transition region plasma, because of O VI lines at 173 Å, but these can become strong enough to be observed by EUVI only when there is a large transition region brightening. Under normal conditions they are lost under the Fe IX-X coronal emission so that the CF cannot be detected with EUVI directly. However, if the CF was due to the appearance of a cold loop system in the SUMER field of view displacing local coronal plasma, EUVI difference images should show a decrease of intensity where this happens, as well as an increase in intensity next to it, due to pile-up of the displaced coronal material. Figure 12 also displays an EUVI difference image taken at the beginning of the life of the CF: a small decrease of the EUVI intensity is present in the SUMER field of view at approximately the same *Y* coordinate of the CF, but no sign of a brightening is present next to it. Moderate dimmings has already started at 22:26 UT, and continued until 22:58 UT. The only explanation supported by Figure 12 is that the local plasma has cooled: its contribution to the total EUVI intensity, although small, vanishes, and at its place cold plasma emits, whose radiation is invisible to EUVI. Such a scenario is also compatible

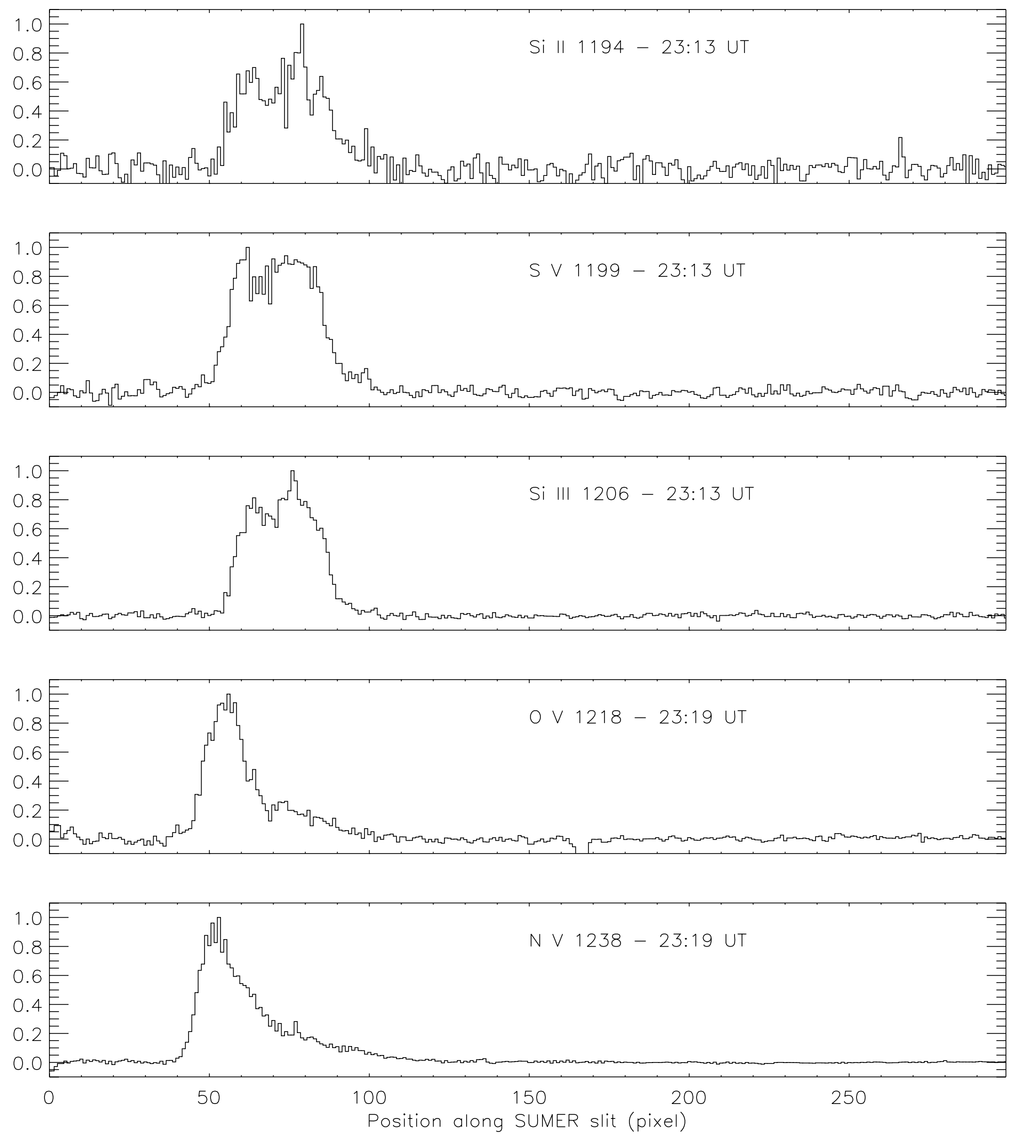

Figure 8. Intensity profiles of lines emitted by the CF versus SUMER pixel position. Pixels 0 and 300 correspond to the north and south edges of the slit, respectively.

with SUMER observations, which show how material in the $5.6 \leqslant \log T \leqslant 5.9$ temperature range (that contributes only moderately to EUVI images) disappears at the locations where the CF is emitting.

We interpret both HF and CF as manifestation of the same phenomenon: a cold plasma component in an active region that suddenly cools down to chromospheric temperatures. The disappearance of the CF at around 23:35 UT is probably due to the cooling plasma slipping out of the SUMER field of view. In fact, had the plasma remained in the same location, it could still have been observed by SUMER, either with lines of ions formed at transition region temperatures, or, had this plasma continued to cool down, with lines at even lower temperatures also available in SUMER. The disappearance of the CF indicates that most likely this plasma has moved out of the SUMER field of view.

4. PLASMA DIAGNOSTICS

4.1. Dynamics

We have measured the line-of-sight velocity of several lines belonging both to the HF and CF in order to determine the dynamical status of the plasmas that emit them. Unfortunately, the EUVI filters did not allow us to detect motions, because of their low sensitivity to plasmas at temperatures in the $5.6 \leqslant \log T \leqslant 5.9$ range.

Spectral line profiles were fitted with a Gaussian function with a least-squares procedure that provide the line centroid in pixels. In order to measure Doppler velocities we need to establish a wavelength scale, since the SUMER spectrum does not have a fixed one. To do this, we have followed two methods. For CF lines, we used their own intensities observed outside the CF. In fact, these lines are too cold to be emitted locally by off-disk plasmas and their intensity is given by scattered light only. Instrument scattered light in SUMER gives rise to an unshifted, average solar spectrum that can be safely assumed to be at rest position. For HF lines, we have assumed that the centroid position measured after averaging the emission of the southward half of the slit (pixels 150–300) is at rest position. This assumption is justified by the lack of any activity in this region.

We used the measurement of the centroid of the "rest" emission of each of the lines we considered, their laboratory rest wavelength, and the known SUMER pixel-to-wavelength relation, to associate an absolute wavelength shift with the

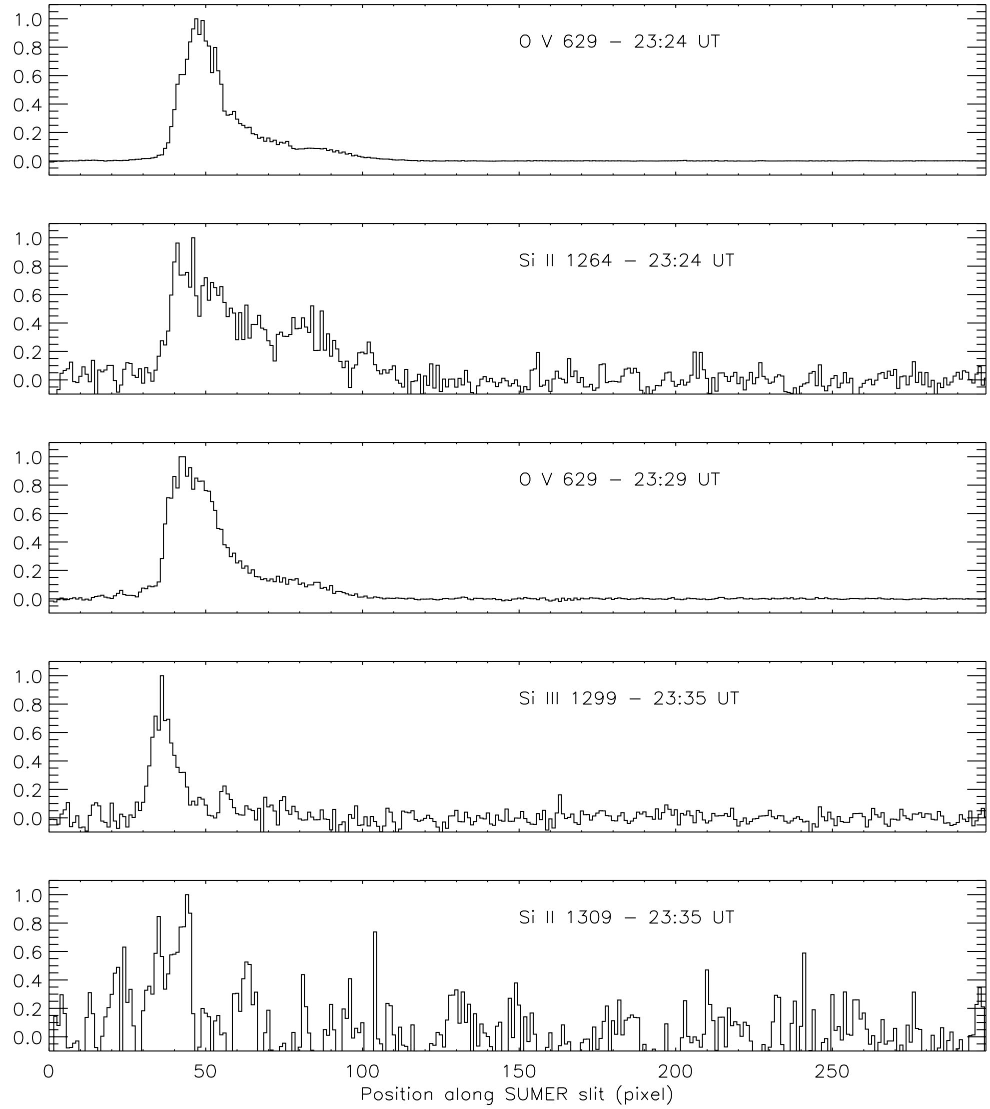

Figure 9. Intensity profiles of lines emitted by the CF versus SUMER pixel position. Pixels 0 and 300 correspond to the north and south edges of the slit, respectively.

measured pixel centroids of HF and CF lines; these have been used to measure line-of-sight velocities.

EIS rest wavelengths also were determined from pixels 150 to 300 of the SUMER portion of the EIS slit. However, line centroids also needed to be corrected for the tilt of the slit relative to the wavelength dispersion direction that shifts wavelengths toward the red from the top to the bottom of the EIS CCD.

We studied HF lines first. We have averaged together the spectra of the pixels in a few subsections of the SUMER and EIS slits corresponding to different portions of the HF: pixels 160–180, 180–200, 200–220, 220–240, 240–260, and 260–280. We considered SUMER lines from Fe VIII, Mg VII,VIII, Ca IX, Ne VII, S VI and Si VII observed from 21:14 UT to 22:41 UT. We find that all speeds are within 10 km s^{-1} and their direction is randomly distributed in different lines and at different locations: no trend is found in any of the lines, at any location and at any time. The same results are found with EIS lines Fe VIII 185.60 Å and Si VII 275.35 Å, the two strongest HF lines in the EIS spectrum. Our data do not show any clear evidence of bulk motions along the line of sight in the HF.

Line-of-sight velocities in the CF could be measured with SUMER only. We summed together the emission of the entire feature, in order to increase signal-to-noise. Also, in order to improve the quality of the measurements, we only considered the brightest lines among the CF ones: He I 584.34 Å, Si III 1206.50 Å, N V 1238.82 Å and O V 629.73 Å. These lines were observed between 23:08 UT and 23:29 UT. Their centroids showed a constant Doppler redshift of approximately 7–10 km s^{-1}, which did not change with time, so that the plasma seems to be constantly moving away from the observer. This result needs to be combined with the velocity in the plane of the sky in order to provide the true velocity of the plasma. Unfortunately, EUVI and EIT could not provide such an estimate because no plasma motion was visible in their images. We had to use the motion of the CF intensity along the SUMER slit. This was measured to be around 12 km s^{-1}, but it only provides the component along the north–south direction. When combined with the line-of-sight speed, the resulting velocity in the plane of the SUMER line of sight and slit is $\approx 14-16$ km s^{-1}. In order to determine the true value of the velocity we need to have some information on the angle between the plane of the SUMER line of sight and slit, and the plane of the loop system that is hosting the CF. Such an angle is not easy to determine. By inspecting EIT images of several days earlier when the active region was on the disk, we can very roughly estimate this angle to be $\approx 45°$. If we assume this value, the velocity is $\approx$ 20–23 km s^{-1}.

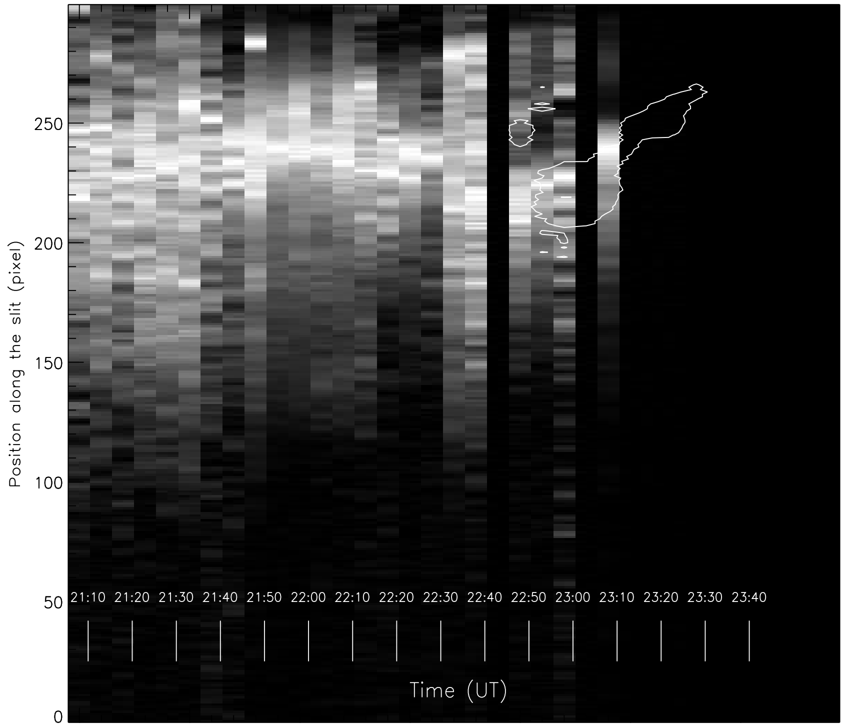

Figure 10. Normalized intensity of the HF as a function of time (along the *X*-axis). This image has been obtained by placing side by side along the *X*-axis the intensity profile along the slit of lines emitted by the HF, each from a different SUMER frame observed at a different time. The *X*-axis is time (in UT) as marked at the bottom of the figure. The *Y*-axis is the position along the SUMER slit, with pixel 0 corresponding to the south direction. The contours of the normalized intensity of the CF are superimposed; contours correspond to half of the maximum intensity.

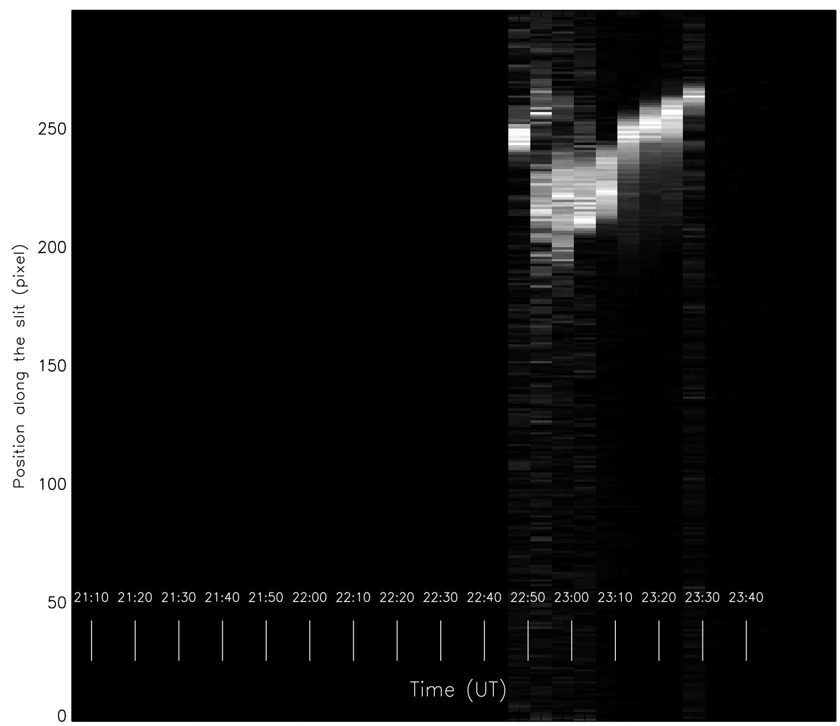

Figure 11. Normalized intensity of the CF as a function of time (along the *X*-axis). This image has been obtained by placing side by side along the *X*-axis the intensity profile along the slit of lines emitted by the CF, each from a different SUMER frame observed at a different time. The *X*-axis is time (in UT) as marked at the bottom of the figure. The *Y*-axis is the position along the SUMER slit, with pixel 0 corresponding to the south direction.

4.2. Diagnostics of the HF

Figures 5 and 10 shows that the HF is relatively stable. It emits the lines listed in Table 1, originating from ions mostly formed at temperatures in the $5.6 < \log T < 5.9$ range, and their normalized intensities do not seem to change from the start of the observations at 21:08 UT until 22:52 UT. Time series of EUVI-A 171 Å difference images with a 2.5 s cadence

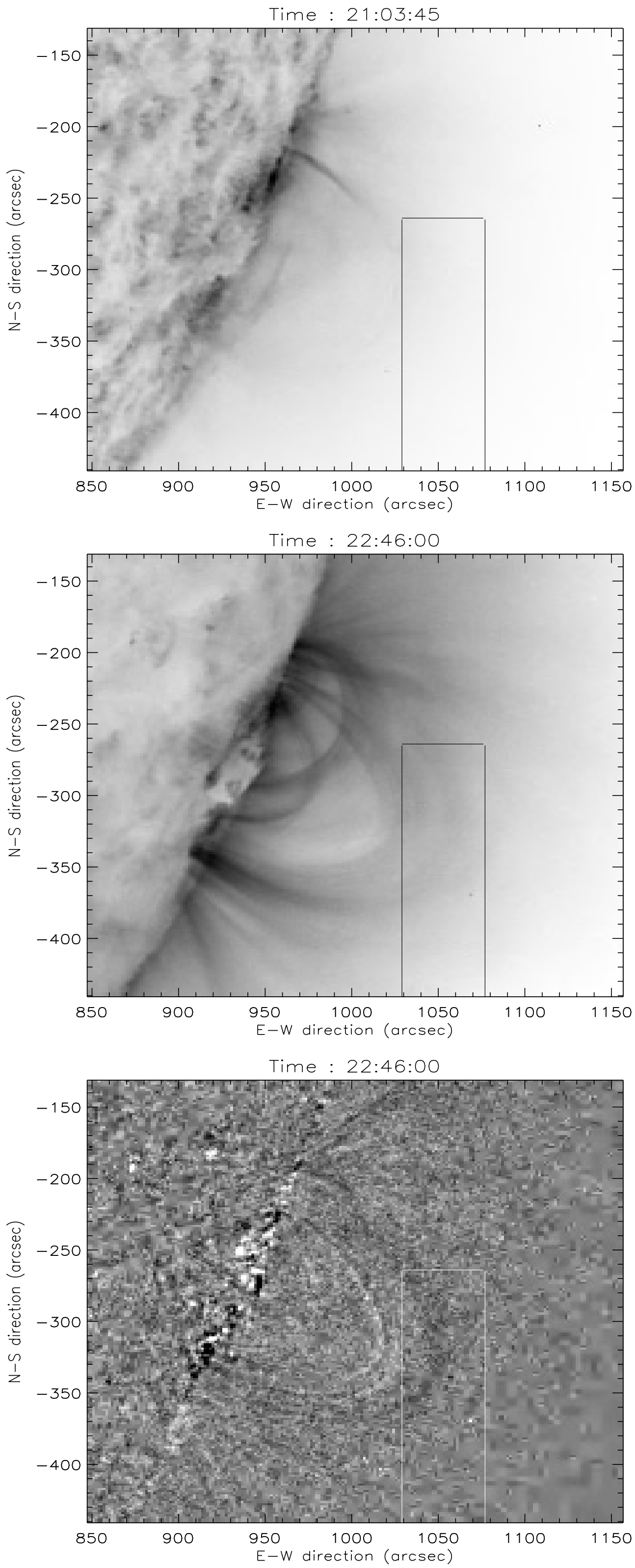

Figure 12. EUVI images of the active region, in the 304 Å (top) and 171 Å (middle) filters, observed at 22:46 UT. The bottom panel displays the difference image of the 171 Å filter at 22:46 UT from the previous one. The rectangle is the top portion of the SUMER slit field of view projected in the plane of the sky seen by EUVI, at the height of the emitting region (see Section 3.2).

also do not show any significant difference in the plasma in the SUMER field of view from the start of the SUMER observation until 22:52 UT. At this time, the normalized intensity profile shows a depletion at around pixels 40-60; no signatures of this plasma are visible after 23:13 UT.

It is to be noted that Mg VI emission, observed at 23:13 UT, could in principle be emitted by either HF, CF, or both, because its intensity distribution along the slit is rather different both from the one from the ions observed earlier and from the CF one. This can be due either to genuine intensity contributions from the CF, or to the cooling and disappearance of HF plasma. It is impossible to distinguish between these two possibilities. In what follows, we have somehow arbitrarily associated Mg VI with the HF, but since it is impossible to distinguish either contribution, this association needs to be taken with caution.

We have carried out the measurements on the entire HF, by summing the emission of pixels 20–140 ("total data set"), as well as to subsections of this structure, obtained summing the emission measured in pixels 20–40, 40–60, 60–80, 80–100, 100–120, and 120–140 (subsets "a," "b," "c," "d," "e," and "f," respectively). By doing this, we tried to capture any possible spatial modulation of the plasma physical properties inside the HF.

We have measured the physical properties of the HF assuming that it is quiescent. This assumption is reasonable for all lines observed until 22:52 UT, but it might be questionable for the pixels where the normalized intensity profiles shows a variation after 22:52 UT, corresponding to subsets "a" and "b."

We have measured the electron temperature and density of the plasma using line intensity ratios, and investigated the thermal structure of the emitting plasma using both an EM loci technique and DEM diagnostic technique. For details on these diagnostic methods, see the review by Phillips et al. (2008). In particular, we have used the Landi & Landini (1997) iterative technique to measure the DEM of the plasma, while we have implemented the line ratio and EM technique in the standard way discussed by Phillips et al. (2008). To carry out plasma diagnostics on the HF, we have used the emissivities of version 5.2.1 of the CHIANTI database (Dere et al. 1997; Landi et al. 2006), adopting the ion fractions of Mazzotta et al. (1998) and the coronal abundances of Feldman et al. (1992).

It is very important to note that both lines from low-FIP elements (i.e., with first ionization potential (FIP) smaller than 10 eV, shown with full lines in Figure 13) and high-FIP elements (FIP>10 eV, dashed lines) are present in the data set. In order to avoid problems related to the FIP effect, we first applied the EM diagnostic technique to intensities of the low-FIP ions, more numerous than the high-FIP ones, assuming coronal abundances. After determining the crossing point, we then included the high-FIP lines.

The application of the EM diagnostic technique has shown that the plasma is nearly isothermal. This is true both for the total data set and for each of the subsets "a" to "f." The measured EM and temperature values for all data sets are listed in Table 3. The emission measure of the plasma changes by a factor $\simeq 1.4$ within the subsets but the uncertainties are larger (0.25 dex) than these differences. The temperature is also fairly constant, and ranges between $\log T = 5.8$ to $\log T = 6.0$ when uncertainties are taken into account. An example of the application of the EM loci technique to the total data set is shown in Figure 13. In this figure, all EM loci curves (one for each line in the data set) cross in the same small area (indicated by vertical and horizontal dashed lines), which provides the EM and temperature values and their uncertainties. The presence of such a small area where the EM loci curves cross indicates that the plasma is nearly

Table 3
Diagnostic Results for the HF

Diagnostics	Ratio	Subsets						Total Data Set
		a	b	c	d	e	f	
log EM		43.80 ± 0.20	43.85 ± 0.20	43.80 ± 0.25	43.75 ± 0.25	43.75 ± 0.25	43.70 ± 0.25	44.50 ± 0.20
log T		5.88 ± 0.05	5.87 ± 0.05	5.87 ± 0.05	5.88 ± 0.05	5.90 ± 0.05	5.93 ± 0.05	5.87 ± 0.06
log T	Ne VII 895.17/ 973.33	$5.96^{+0.20}_{-0.13}$	$5.67^{+0.12}_{-0.08}$	$5.75^{+0.14}_{-0.10}$	$5.94^{+0.22}_{-0.13}$	$5.76^{+0.15}_{-0.10}$	$5.76^{+0.15}_{-0.10}$	$5.79^{+0.16}_{-0.10}$
	Ne VI 558.69/ 997.03	5.61 ± 0.10	5.24 ± 0.08	5.54 ± 0.10	6.00 ± 0.13	6.08 ± 0.14	5.94 ± 0.14	5.68 ± 0.11
	Ne VI 558.69/ 999.18	5.95 ± 0.18	5.20 ± 0.07	5.50 ± 0.10	6.10 ± 0.12	6.12 ± 0.12	5.97 ± 0.12	5.72 ± 0.15
	Ne VI 558.69/1005.69	5.90 ± 0.12	5.19 ± 0.07	5.45 ± 0.10	6.21 ± 0.12	6.11 ± 0.11	5.81 ± 0.13	5.70 ± 0.14
	Ne VI 562.70/ 997.03	5.46 ± 0.10	5.29 ± 0.08	5.51 ± 0.10	5.88 ± 0.13	6.00 ± 0.13	5.99 ± 0.14	5.62 ± 0.10
	Ne VI 562.70/ 999.18	5.70 ± 0.14	5.25 ± 0.08	5.46 ± 0.10	5.96 ± 0.17	6.03 ± 0.16	6.02 ± 0.17	5.64 ± 0.13
	Ne VI 562.70/1005.69	5.69 ± 0.13	5.24 ± 0.07	5.42 ± 0.09	6.08 ± 0.14	6.02 ± 0.14	5.88 ± 0.15	5.64 ± 0.13
log N_e	Fe VIII 697.16/721.26	> 8.6	> 8.3	> 7.7	> 7.9	> 7.7	> 8.0	> 8.0
	Mg VIII 762.66/772.26	< 8.2	9.0 ± 2.1	< 10.0	9.0 ± 2.1	< 11.2	< 10.0	< 10.0
	Mg VIII 789.41/772.26	< 7.3	7.35 ± 0.35	7.15 ± 0.25	7.1 ± 0.3	7.8 ± 0.7	7.35 ± 0.35	7.35 ± 0.35
	Al VII 1053.99/1056.92	$8.9^{+1.0}_{-1.2}$	< 9.7	< 9.6	< 9.5	< 9.6	< 9.6	< 9.7
	Mg VI 1190.12/1191.67	> 9.75	9.0 ± 0.3	$9.3^{+0.3}_{-0.4}$	$9.20^{+0.2}_{-0.4}$	$9.30^{+0.3}_{-0.4}$	$9.50^{+0.4}_{-0.3}$	$9.30^{+0.3}_{-0.4}$
	Fe VIII 186.60/185.21	> 7.6	8.0 ± 0.5	8.2 ± 0.6	8.0 ± 0.5	7.9 ± 0.4	8.0 ± 0.5	8.0 ± 0.5

isothermal. There are, however, two lines that do not cross this small area, emitted by Al VII: the atomic model is limited to the three lowest configurations and does not include resonant excitation, so the emissivities of Al VII lines are of limited accuracy.

When we added the high-FIP ions (shown as dashed curves in Figure 13), we found that Ne VII and S VI also cross the common point (thus confirming the coronal abundance assumption), while all Ne VI curves are too high, and require photospheric abundances. This leaves the question open of the element composition of HF plasma, and since the low-FIP abundances change by a factor of 4 between coronal and photospheric values, also the absolute value of the EM suffers from the same uncertainty.

We have applied the Landi & Landini (1997) DEM diagnostic technique to the low-FIP lines of all data sets in order to check the results of the EM loci technique. In all cases, the spectral lines were able to provide information on the emitting plasma only in the restricted temperature range around log $T = 5.8$–5.9, and were roughly consistent with an isothermal picture. However, the lack of HF lines formed at different temperature ranges did not allow us to put any constrain to either the low-temperature and the high-temperature sides of the EM. This lack of lines further confirms that the temperature of the HF plasma is limited to a narrow range of values.

Since the plasma is approximately isothermal, the application of the line intensity ratios will provide the temperature and the density of the emitting plasma. Results are reported in Table 3. The SUMER spectra allowed us to measure the plasma electron temperature using intensity ratios of lines emitted by Ne VI and Ne VII, and the electron density using a Mg VI line pair. However, it is to be noted that the intensities of Mg VI and of the Ne VI 558.69 Å and 562.70 Å lines were observed after 22:52 UT. These two ions are the coldest of the data set and might be influenced by the CF, and indeed the normalized intensities of their lines depart from the behavior of the other lines emitted by the HF, as shown in Figure 5. The diagnostic results obtained using these lines need to be taken with caution for subsets "b" and "c," corresponding to the locations of the CF.

The electron temperature measured with the Ne VII line ratio is in agreement with the results obtained with the EM loci technique, except in subset "b" where the difference between its temperature and the EM loci value is larger than the uncertainties. Ne VI-based temperatures for subsets "d" to "f" indicate coronal values at around 1 MK. Considering their error bars and the scatter given by each line ratio within each subset, the Ne VI temperatures are in fairly good agreement with the EM results. Subsets "b" and "c" indicate much lower temperatures, and this is most likely due to contamination from the CF. Those results need to be taken with caution. The results for subset "a" show significant scatter, their behavior is unclear.

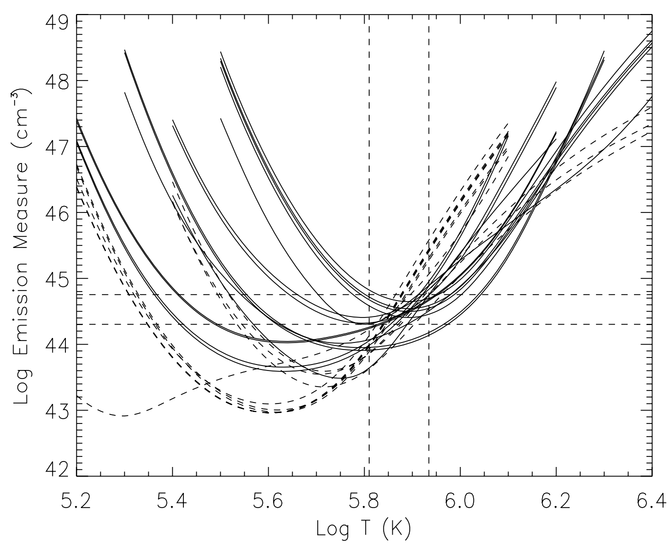

Figure 13. EM loci technique applied to the intensities measured over the entire HF ("total data set"). Full lines indicate the EM loci curves of ions with first ionization potential (FIP) smaller than 10 eV; dashed lines are used for lines of ions with FIP>10 eV. A crossing point can be seen at around log $T \simeq 5.85$, from which the plasma temperature and EM are measured. Two lines from Al VII miss this crossing point and they are discussed in the text.

The electron density measurements were carried out using the few density sensitive line ratios available in SUMER and EIS for HF ions. We used ratios from Fe VIII, Mg VI, Al VII, and Mg VIII to measure the electron density, and results are listed in Table 3. We did not use the Mg VI 268.99/270.40 ratio because of the difficulty of separating the 270.40 Å line from the blending Fe XIV line at 274.52 Å. We included excitation from background photospheric radiation into the calculation of the theoretical intensity ratios because the electron density is sufficiently low to make this process non-negligible when compared to electron impact excitation. The effects of photoexcitation are to decrease the ratio density sensitivity at low densities. This is the main cause of the rather loose limits to the electron density provided by the ratios listed in Table 3. All ratios point toward a low density, and a value on the order of $\log N_e \approx 8.0 - 8.5$ that satisfies all results except those from the Mg VIII 789.41/772.26 ratio which indicate a much lower density. The Mg VI 1190.12/1191.67 ratio shows higher densities at all locations, more similar to CF densities (see below), suggesting that HF plasma is actually condensing and increasing its density as it cools down. However, we monitored the density measurements obtained with EIS and found that they were constant with time between 19:30 UT and 23:00 UT.

4.3. Diagnostics of the CF

CF plasma significantly changes with time so plasma diagnostics needs to be carried out only using lines observed simultaneously. This limits severely our results, since only two or three ions at maximum are found in each SUMER frame that belong to this feature. We have mostly relied on line intensity ratios to measure—where possible—the electron temperature and density of the plasma. In one case, we even tried to estimate the emission measure of the emitting plasma and its abundance composition. In all cases, we have not tried to differentiate among different sections of the CF, but we have summed all of its emission. This was made necessary by the small size of the structure and by the limited signal-to-noise ratio of many of the lines emitted by it. Results are listed in Table 4.

The first thing to note is that the plasma is either multithermal, or it is strongly out of equilibrium. In fact, an isothermal plasma could not emit at the same time Si II, Si III and C III on one side, and O IV, O V and N V on the other, as these ions, under equilibrium conditions, are formed at temperatures almost one order of magnitude apart. The temperature diagnostics seems to confirm this, because Ne V and O V line ratios indicate a temperature in the 1.1–2.0$\times 10^5$ K range, while Si II/Si III line ratios indicate a temperature on the order of 4×10^4 K. It is interesting to note that the temperature measured by the Si ions is approximately constant with time, while the one provided by Ne and O ions seems to decrease with time.

The electron density of the CF can be estimated only through C III line ratios, observed in two subsequent SUMER frames. These ratios indicate a rather low electron density at 23:08 UT, on the order of 10^9 cm^{-3}, typical of quiescent active regions. If coupled to the temperature values measured by the Si ions (closer to the temperature of formation of C III lines), this density yields a pressure of 0.0055 dyn cm^{-2}. The electron density seems to have increased at 23:13 UT, and only a lower limit can be given. The density values are larger than those measured in the HF, except for the Mg VI values which agree with the CF ones.

4.4. Emission Measure and Element Abundances

Knowing the electron density and temperature from Si II, Si III C III, we can estimate the EM and the relative abundance of C and Si. Even though the plasma is likely multithermal, we can assume that Si II, Si III, and C III are formed at similar temperatures, because the temperature measured from the Si ions is close to the temperature of maximum abundance of both Si III and C III. We have used the measured temperature and density values, CHIANTI version 5.2.1 emissivities, the Mazzotta et al. (1998) ion abundances, and the photospheric element abundances from Grevesse & Sauval (1998), to calculate the emission measure from each line. To minimize uncertainties in the fitting of each C III line, which are bundled together in SUMER spectrum, we have summed up all the counts of the entire C III multiplet. The resulting EM values are listed in Table 4. The ratio between the two EM values provides a check on the relative abundance of the elements, since such a ratio is proportional to the element abundance.

The agreement between the EM values obtained with C and Si indicate that the plasma element composition is photospheric: its FIP bias is unity within uncertainties. This result leads us to speculate on two possible scenarios. In the first scenario, the CF plasma is mostly due to evaporation of photospheric material along loops, that started to cool dramatically once it reached a certain critical density. However, velocities before the rise of the CF were so low that the local plasma does not seem to be replenished by such upflows. In the second scenario, the cooling plasma was already present in the coronal loops before cooling took place. This implies that also the HF plasma should have photospheric abundances. Unfortunately, we could not determine them unambiguously, in order to check this possibility. If the HF plasma abundances are indeed photospheric, then the EM values listed in Table 3 should be increased by a factor of 4 (or 0.6 dex) to reach a value of $\log EM = 45.1$ for the total data set, and $\log EM \approx 44.3$–44.4 for each individual subset.

4.5. Filling Factor

The ability of EUVI of observing the field of view from a different direction allows us to reconstruct the geometry of the emitting region and to determine its volume. Using the density measurements obtained from line ratios we could calculate the expected EM of the emitting region that, when compared to the one derived from line intensities, allows us to determine the filling factor of the emitting region.

The size of the slit covered by the CF is approximately 50″ long. Since 1″ corresponds to 720 km at Earth's distance, the

Table 4
Diagnostic Results for the CF

Time (UT)	Ion	Diagnostics	Result
22:57	Ne V	572/1145	$\log T = 5.32 \pm 0.10$
23:02	Ne V	572/1145	$\log T = 5.15 \pm 0.08$
		569/1145	$\log T = 5.15 \pm 0.08$
23:08	C III	1174.8/1175.9	$\log N_e = 8.95 \pm 0.25$
		1175.2/1175.9	$\log N_e = 8.95 \pm 0.30$
		1175.5/1175.9	$\log N_e = 9.05 \pm 0.30$
		1176.3/1175.9	$\log N_e = 9.25 \pm 0.35$
23:13	C III	1174.8/1175.9	$\log N_e > 9.4$
		1175.2/1175.9	$\log N_e > 9.5$
		1175.5/1175.9	$\log N_e > 9.9$
		1176.3/1175.9	$\log N_e > 9.5$
	Si II, III	1193/1206	$\log T = 4.61 \pm 0.03$
		1194/1206	$\log T = 4.62 \pm 0.03$
	Si II, III		$\log EM_{Si} = 44.6 \pm 0.1$
	C III		$\log EM_C = 44.65 \pm 0.2$
		EM_{Si}/EM_C	FIP = 0.89 ± 0.25
23:19	O V	1218/629	$\log T = 5.05 \pm 0.07$
23:35	Si II/III	1309/1294	$\log T = 4.56 \pm 0.02$
		1309/1299	$\log T = 4.54 \pm 0.02$
		1309/1303	$\log T = 4.56 \pm 0.02$

area of the CF included in the SUMER slit field of view is $S = 1.0 \times 10^{18}$ cm^{-2}. Figure 12 shows that the size of the cooling region in EUVI's plane of the sky is $\approx 20''$ wide. If we assume that the cooling region is a toroidal loop system, the total volume of the plasma emitting the SUMER line intensities is $V = 1.5 \times 10^{27}$ cm^3. Using the measured electron density, the expected EM value is $EM_{\rm exp} = 1.5 \times 10^{45}$ cm^{-3}. When compared to the measured EM value (see Table 4), we find that the filling factor is $f \approx 0.3$.

It is more difficult to estimate the volume of the HF, since no clear signature of it can be identified with EUVI. Also, the uncertainty about element abundances and electron density makes such an estimate even more difficult to make. If we assume that the HF is also made of the same loops with the same thickness as the CF, and use a density value of $\log N_e = 8.5$, we can estimate the EM value of each $20''$ long subsection of the slit to be $\log EM \approx 43.8$ which means a filling factor of near unity for each subset.

5. SUMMARY

In the present work, we reported on the coordinated EIS, EIT, EUVI, LASCO, SUMER, and UVCS observations of a cooling loop system located in active region 10989 just behind the west limb. We used EIS and SUMER to determine the plasma physical properties, measuring dynamics, thermal structure, emission measure, element abundances, electron density and temperature, and, with the help of EUVI also the volume and filling factor of the plasma before and during the cooling event. We used UVCS to observe the evolution of coronal emission above the active region. No streamer structure was observed associated with AR 10989 at a position angle between 242° and 253°.

Our measurements are consistent with a scenario where a bundle of quiescent cool loops, embedded side by side to hotter loops in the active region, suddenly begins to rapidly cool down and form a condensation. This condensation is characterized by a steady and slow motion along the loop magnetic field lines, and is made of plasma likely outside of equilibrium, of lower temperature and larger electron density than the original quiescent cool loops. This condensation eventually slips away from the SUMER and EIS fields of view, and after that no trace is left of the original loop system. This scenario depends on the element abundances of the CF and HF plasma. In fact, rapid cooling and condensation of local coronal plasma require that both the initial and final plasmas have the same abundances. In the present study, we could only determine the abundances of CF plasma, but not those of the HF plasma. The former are photospheric, while the latter are undetermined. This cooling loop scenario needs thus to be confirmed.

This scenario is broadly consistent with the theoretical models of loop condensations developed by Karpen & Antiochos (2008) and references therein, where footpoint heating drives evaporation of chromospheric material into coronal loops, which eventually causes catastrophic cooling and condenses into prominence-like material. The present measurements provide for the first time detailed plasma diagnostics that will allow us to test such models in great detail, by comparing the measured physical parameters of the emitting plasma with observables predicted by the models. The present results are the first of the kind to be published: while condensing loops have been observed many times in the past, instrumental limitations had so far prevented detailed plasma diagnostics of the cooling plasma before and during the cooling phase. We plan to carry out detailed and extensive comparisons of model predictions with the present measurements in a subsequent paper.

The present results, however, still suffer from several limitations that call for improvements in future observations. Plasma diagnostics could be carried out only for limited number of times during the observations, so that no time-resolved diagnostics was possible. Element abundances are a key parameter to understand whether the HF and CF were actually made of the same plasma, yet HF diagnostics did not provide a definitive result. Time resolution (5 minutes at best) was low, and the number of lines observed by SUMER was too limited to allow us to measure the evolution of the CF in detail. Therefore, the present work marks a big step forward toward providing adequate experimental tests to theoretical models of condensation formation; yet, more work and more observations are required to provide a more comprehensive and time resolved data set.

The work of E.L. is supported by the NNG06EA14I, NNH06CD24C and other NASA grants. The work of M.P.M. is supported by NASA grants NNX06AG95G and NNX08AQ96G to the Smithsonian Astrophysical Observatory. The ground-based polarization brightness images used here were produced by the High Altitude Observatory's Mauna Loa Observatory. The space-based images in Figures 1 and 2 are courtesy of the EIT and LASCO/*SOHO* consortia. The SUMER project is financially supported by DLR, CNES, NASA, and the ESA PRODEX programme (Swiss contribution). SUMER is part of *SOHO* of ESA and NASA. The authors thank S. R. Cranmer for valuable discussions, and the anonymous referee for his/her comments that helped improve the original manuscript.

REFERENCES

Brown, C. M., Feldman, U., Seely, J. F., Korendyke, C. M., & Hara, H. 2008, ApJ, 176, 511

Culhane, J. L., et al. 2007, Sol. Phys., 243, 19

De Groof, A., Bastiaensen, C., Müller, D. A. N., Berghmans, D., & Poedts, S. 2005, A&A, 443, 319

De Groof, A., Berghmans, D., van Driel-Gesztelyi, L., & Poedts, S. 2004, A&A, 415, 1141

Dere, K. P., Landi, E., Mason, H. E., Monsignori Fossi, B. C., & Young, P. R. 1997, A&AS, 125, 149

Feldman, U., Landi, E., Doschek, G. A., Dammasch, I. E., & Curdt, W. 2003, ApJ, 593, 1226

Feldman, U., Mandelbaum, P., Seely, J. L., Doschek, G. A., & Gursky, H. 1992, ApJS, 81, 387

Galsgaard, K., & Longbottom, A. W. 1999, ApJ, 510, 444

Gardner, L. D., Atkins, N., Fineschi, S., Smith, P. L., Kohl, J. L., Maccari, L., & Romoli, M. 2000, Proc. SPIE, 4139, 362

Gardner, L. D., et al. 1996, Proc. SPIE, 2831, 2

Gardner, L. D., et al. 2002, The Radiometric Calibration of *SOHO* (ESA SR-002), ed. A. Pauluhn, M. C. E. Huber, & R. von Steiger (Noordwijk: ESA), 161

Grevesse, N., & Sauval, A. J. 1998, Space Sci. Rev., 85, 161

Hara, H., Nishino, Y., Ichimoto, K., & Delaboudiniere, J.-P. 2006, ApJ, 648, 712

Karpen, J. T., & Antiochos, S. K. 2008, ApJ, 676, 658

Karpen, J. T., Antiochos, S. K., Hohensee, M., & Klimchuk, J. A. 2001, ApJ, 553, L85

Karpen, J. T., Antiochos, S. K., Klimchuk, J. A., & MacNiece, P. J. 2003, ApJ, 593, 1187

Kjeldseth Moe, O., & Brekke, P. 1998, Sol. Phys., 182, 73

Kohl, J. L., Noci, G., Cranmer, S. R., & Raymond, J. C. 2006, A&A Rev., 13, 31

Kohl, J. L., et al. 1995, Sol. Phys., 162, 313

Kohl, J. L., et al. 1997, Sol. Phys., 175, 613
Kohl, J. L., et al. 1999, ApJ, 510, L59
Landi, E., Del Zanna, G., Young, P. R., Dere, K. P., Mason, H. E., & Landini, M. 2006, ApJS, 162, 261
Landi, E., & Feldman, U. 2008, ApJ, 672, 674
Landi, E., & Landini, M. 1997, A&A, 327, 1230
Landi, E., & Landini, M. 2004, ApJ, 608, 1133
Levine, R. H., & Withbroe, G. L. 1977, Sol. Phys., 51, 83
Mazzotta, P., Mazzitelli, G., Colafrancesco, S., & Vittorio, N. 1998, A&AS, 133, 403
Miralles, M. P. 2008, Eos Trans. AGU, 89 (23), Joint Assembly Suppl, abstract SH53A-04
Muglach, K., Landi, E., & Doschek, G. A. 2009, ApJ, submitted
Nagata, S., et al. 2003, ApJ, 590, 1095
O'Shea, E., Banerjee, D., & Doyle, J. G. 2007, A&A, 475, L25
Phillips, K. J. H., Feldman, U., & Landi, E. 2008, in Cambridge Astrophysics Ser. 44, Ultraviolet and X-ray Spectroscopy of the Solar Atmosphere (Cambridge: Cambridge Univ. Press)
Priest, E. R., van Ballegooijen, A. A., & MacKay, D. H. 1996, ApJ, 460, 530
Schmieder, B., Heinzel, P., Wiik, J. E., Lemen, J., Anwar, B., Kotrc, P., & Hiei, E. 1996, Sol. Phys., 156, 337
Schmieder, B., Rust, D. M., Georgoulis, M. K., Demoulin, P., & Bernasconi, P. N. 2004, ApJ, 601, 530
Schrijver, C. J. 2001, Sol. Phys., 198, 325
Svestka, Z. 1987, Sol. Phys., 108, 411
Wang, Y.-M. 1999, ApJ, 520, L71
Wilhelm, K. 1995, Sol. Phys., 162, 189
Winebarger, A. R., & Warren, H. P. 2005, ApJ, 626, 543